UNIVERSITÀ
DEGLI STUDI
DI PADOVA

Dipartimento di Fisica e Astronomia Galileo Galilei
Tesi per il Corso di Laurea Magistrale in Fisica

Beam dynamics studies and optimization of the SuperB Injection System

Relatore:
Prof. Roberto Stroili

Correlatrice:
Dott.sa Susanna Guiducci

Laureando:
Dario Pellegrini

Anno Accademico 2012

to Alessandra,
for making every day a better day.

CONTENTS

PRESENTAZIONE

Lo scopo principale di questa tesi è lo studio della dinamica dei fasci nel sistema di iniezione di SuperB.

SuperB è un collisore asimmetrico di leptoni operante all'energia di centro di massa della $\Upsilon(4S)$ con una luminosità di $10^{36} cm^{-2} s^{-1}$ [1]. Per mantenere costante una così alta luminosità, è necessaria un'iniezione continua ad alta efficienza $\sim$ 99% nei due anelli del collisore. Il sistema di iniezione è composto dalle sorgenti di elettroni e positroni, da uno stadio di accelerazione ad 1 GeV, da un damping ring che riduce l'emittanza ai bassi valori richiesi ed, infine, da un Linac in banda S che accelera i leptoni alle energie degli anelli. All'uscita del damping ring l'estensione longitudinale del pacchetto eccede rispetto al periodo dei campi acceleranti del Linac. E' perciò necessario aggiungere un sistema di compressione che riduca la lunghezza dei pacchetti in modo che durante l'accelerazione, la variazione di momento interna al pacchetto assuma valori accettabili per l'iniezione negli anelli principali.

Lo studio qui presentato include l'ottimizzazione del compressore, la messa a punto dei sistemi necessari al trasporto dei due fasci dal damping ring alla fine del Linac, una simulazione completa per propagare la distribuzione del fascio attraverso il sistema, considerando gli effetti di dinamica del fascio, e la discussione dell'iniezione negli anelli principali.

Nel Capitolo 1 viene presentata la motivazione fisica, seguita da una breve descrizione della macchina e del sistema di iniezione.

La prima parte del Capitolo 2 illustra i concetti del trasporto e ne analizza le principali caratteristiche richieste per questo studio. Viene poi introdotto il concetto di Radiazione di Sincrotrone con un occhio di riguardo per la parte coerente. Infine sono esposti i metodi per trattare i campi scia che interessano il Linac.

Il Capitolo 3 è dedicato al sistema di compressione. Inizia con una descrizione del principio di funzionamento e dei parametri del compressore di SuperB. Questo lavoro è basato su uno studio analitico fatto da Antoine Chancé [2, 3], ed include le aggiunte e le modifiche necessarie per adattare il sistema alla sua configurazione finale. Per eseguire una simulazione completa, il lattice è stato implementato tramite il codice *elegant* [4]. Sono state prodotte simulazioni numeriche della distribuzione

6-dimensionale includendo gli effetti della radiazione di sincrotrone coerente e dei campi scia.

Il trasporto del fascio attraverso il Linac è trattato nel Capitolo 4. Il lavoro include il disegno del lattice necessario ad ottenere l'adeguato focheggiamento del fascio e lo studio degli effetti dei disallineamenti insieme ad uno schema efficace di correzione dell'orbita.

L'ottimizzazione del sistema completo è descritta nel Capitolo 5 dove viene illustrata la scelta del punto di lavoro del compressore assieme agli effetti che i campi scia nel Linac hanno sulla distribuzione finale.

Infine, nel Capitolo 6 è presentata ed analizzata l'iniezione degli elettroni nel Low Energy Ring. Si conclude che la distribuzione finale del pacchetto soddisfa i requisiti per l'iniezione negli anelli principali di SuperB

OVERVIEW

The main purpose of this thesis is the study of the beam dynamics in the injection system of the SuperB project.

SuperB is an asymmetric lepton collider operating at the $\Upsilon(4S)$ centre of mass energy with a luminosity of $10^{36} cm^{-2} s^{-1}$ [1]. Continuous injection in the two rings of the collider, with high efficiency $\sim$ 99%, is needed to keep nearly constant such a high luminosity. The injection system is composed by electrons and positrons sources, a 1 GeV acceleration stage, a damping ring reducing the emittances to the very low values required and, finally, an S-band Linac to accelerate the leptons to the ring energies. At the exit of the damping ring the longitudinal extension of the bunch is large with respect to the period of the Linac accelerating fields. It is therefore necessary to add a bunch compressor system to shorten the bunch length so that during the acceleration, the energy spread is reduced to values that are acceptable for the injection in the main rings.

The study presented here includes the optimization of the bunch compressor, the finalization of the systems needed to transport the two beams from damping ring to the end of the Linac, a start-to-end simulation to propagate the bunch distribution through the system, taking into account all the beam dynamics effects, and the discussion of the injection in the main rings.

In Chap. 1 the physical motivation is presented, followed by a brief description of the machine and the injection system.

The first part of Chap. 2 illustrates the concepts of transport and analyses its main features needed for this study. The concept of Synchrotron Radiation is then introduced with a particular attention to the coherent part of it. Finally the method to treat wake fields in the Linac accelerating sections is exposed.

Chap. 3 is dedicated to the bunch compressor system with a description of its principle of operation and of the parameters of the SuperB one. This work is based on an analytic study made by Antoine Chancé [2, 3], and includes the additions and modifications needed to adapt the system to the final configuration. In order to perform the start-to-end simulation, the lattice has been implemented in the code *elegant* [4]. Nu-

merical tracking of the 6D bunch distribution, including the Coherent Synchrotron Radiation and Wakefields effects, has been produced.

The beam transport through the Linac is treated in Chap. 4. The work includes the design of the lattice to achieve the proper beam focusing and the study of the effects of elements misalignment together with an effective orbit-correction scheme.

The optimization of the full system is then described in Chap. 5 where the choice of the working point of the compressor is illustrated together with the effects of the wakefields of the Linac accelerating section on the final bunch distribution.

Finally the injection of the electrons in the Low Energy Ring is presented and analysed in Chap. 6. The conclusion is that the final bunch distribution satisfies the requirements for injection into the SuperB main rings.

1 INTRODUCTION

One of the biggest unanswered questions of our times is why everything in the Universe is made by matter while high-energy phenomena produce both matter and antimatter in the same quantity.

The answer for this question may be searched in rare phenomena which violate $\mathcal{CP}$. Very precise data came with the measurements of mixing-dependent $\mathcal{CP}$-violating asymmetries in the B meson systems made at BaBar [5] and Belle [6]. The Unitary Triangle construction provides strong self-consistency tests of the three generation Standard Model which were accomplished also with measurements of the B_s mixing made by CDF [7].

The fact that CKM phases have now been shown to be consistent with all observed $\mathcal{CP}$-violating phenomena leads the Standard Model to exclude the possibility of an electroweak baryogenesis. The still possible mechanisms that can explain the asymmetry are: leptogenesis and bariogenesis coming from new $\mathcal{CP}$-violating phases which naturally arise in many extensions of the Standard Model.

Data acquired by the present B-factories are statistically limited and many improvements could be made in the Unitary Triangle with more data in B, D and τ decays. However to touch the limit allowed by theoretical uncertainties, more accurate measurements are required in $\mathcal{CP}$ asymmetries, rare decay branching fractions, and rare decay kinematic distributions in penguin-dominated $b \to s$ transitions. In a word, a level where there is substantial sensitivity to New Physics effects must be reached.

SuperB, having an initial luminosity of 10^{36} $cm^{-2}s^{-1}$, will collect 75 ab^{-1} in five years, more than thirty times the data collected up to now. Such a huge data sample will make the Unitarity Triangle tests, in their manifold versions, the ultimate precision tests of the flavour sector of the Standard Model, and open up the world of New Physics effects in very rare B, D, and τ decays.

SuperB will also collect an unprecedented number of events related to the charm quark which will lead to the detailed exploration of new charmonium states. The great number of τ lepton produced will allow the search for lepton-flavour-violating decays. The accelerator design

will allow for longitudinal polarization of the e^- beam, making possible uniquely sensitive searches for a τ electric dipole moment, as well as for $\mathcal{CP}$-violating τ decays [8].

1.1 THE SUPERB PROJECT

SuperB is an asymmetric electron positron collider operating at an energy of the centre of mass equal to 10.58 GeV and aiming at a luminosity of 10^{36} $cm^{-2}s^{-1}$. The target luminosity is about two orders of magnitude larger than the luminosity achieved by the PEP-II (SLAC, USA) and the KEKB (KEK, Japan) colliders. The leptons are stored in two rings (e^+ at 6.7 GeV, e^- at 4.2 GeV) intersecting with a crossing angle at the interaction point. The design is based on a "large Piwinski angle and Crab Waist" scheme [9, 10, 11] already successfully tested at the DAFNE Φ-Factory in Frascati, Italy. This scheme allows reaching very high luminosity by reducing the beam sizes at the interaction point, while the beam currents are voluntarily kept low to contain the power consumption and operating costs. The project combines the challenges of high luminosity colliders and state-of-the art synchrotron light sources, in order to achieve extremely low emittances and small beam sizes at the interaction point. As unique features, the electron beam will be longitudinally polarized at the IP and the rings will be able to ramp down to collide at the τ/charm energy threshold.

The SuperB collider project has been approved by the Italian Government as part of the National Research Plan and will be built by the Cabibbo Lab in the campus of Tor Vergata University, Rome, just 5 Km away from the INFN Frascati National Laboratories. The layout of the SuperB accelerator complex is shown in Fig. 1.1 below. The two rings have an equal circumference of $\sim$ 1200 m and very similar small emittance lattices, inspired to those of modern SR sources.

The original design, described in detail in a revised edition of the Conceptual Design Report [8], has been lately reviewed in order to meet the requirements of the new site [12]. Some Synchrotron Radiation beam lines were foreseen for a future use of SuperB as a synchrotron light source, however at the moment this option is not accounted for the first phase. A recent development is the option to use the high energy Linac for a SASE-X-FEL [13] in parasitic mode to the collisions. Work is in progress to exploit the design and evaluate possible issues.

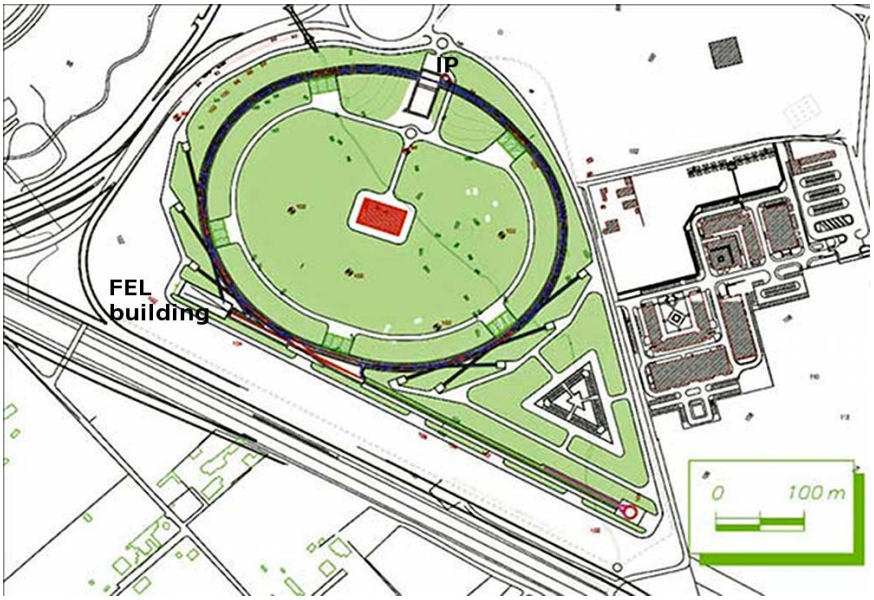

Figure 1.1. *Footprint of the layout of the SuperB project at Cabibbo Lab.*

1.2 INJECTION SYSTEM

SuperB injection system delivers full energy, low emittance beams to the main rings: 4.2 GeV electrons for the Low Energy Ring (LER) and 6.7 GeV positrons for the high Energy Ring (HER). The injection has been designed to be continuous in order to keep nearly constant beam current and luminosity [14].

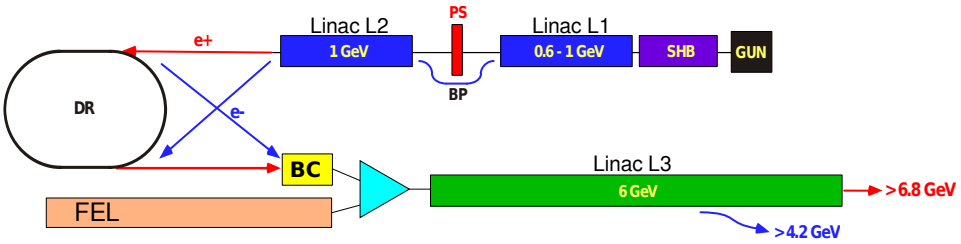

Figure 1.2. *Scheme of the injection system of SuperB.*

A scheme of the injection system is presented in Fig. 1.2. The system consists of a polarized electron gun, a positron production system, electron and positron Linac sections, a damping ring and the transfer lines connecting these systems to the collider main rings.

The gun which produces the electrons is like the one used by the SLC collider at SLAC, where a polarization of 80% has been routinely

achieved [15]. The gun produces a single electron bunch (or a short train of up to 5 bunches), with up to 10 nC charge. The immediately downstream section rotates the polarization in the vertical plane.

To effectively compensate for the losses of the main ring, the charge required for injection is 300 pC/bunch. A small train of 5 bunches will be inject with a repetition cycle of 30 ms for each beam. The high charge provided from the gun is needed for the production of the positrons since the electron-positron conversion efficiency is of the order of a few percent [16].

For the injection into the Low Energy Ring, electrons accelerated up to 1 GeV in Linac L1, are stored into the DR to reduce the emittance. For HER injection electrons accelerated in Linac L1, are focused on a tungsten target to produce pairs e^+e^- by bremsstrahlung. After the converter, the positrons are collected and accelerated up to 1 GeV in Linac L2 before the injection in the damping ring. Two pulsed magnets are used to bypass the target in the electron injection cycles.

Electron and positron beams are alternatively stored in the damping ring for 10 and 20 ms respectively (see Fig. 1.3) in order to reduce the beam emittance, through the radiation damping mechanism, to the value required for main ring injection. At the damping ring exit a bunch compressor reduces the length of both the electron and positron bunches in order to accelerate them in the Linac L3 (the main one) without producing big energy spread that would not be acceptable for main ring injection. Linac L3 is based on S-band, SLAC type, accelerating sections operating at a repetition frequency of 100 Hz; it accelerates the two beams up to the main rings energies: 4.18 GeV for electrons and 6.7 GeV for positrons.

The injection repetition cycle is 30 ms for each beam. This timing scheme allows to accelerate in Linac L3 a beam pulse for a SASE FEL facility, during the store time of the positrons in the DR, without affecting the injection rate for SuperB (see Fig. 1.3); however studies are still ongoing on this subject. The beam for the SASE FEL would be produced by a dedicated high brightness photoinjector similar to that used at LNF in the SPARC-LAB facility [17], accelerated up to 0.7 GeV and then injected, into the Linac L3. A pulsed magnet will be used to combine the FEL beam with the SuperB injection beams.

1.2.1 Damping Ring

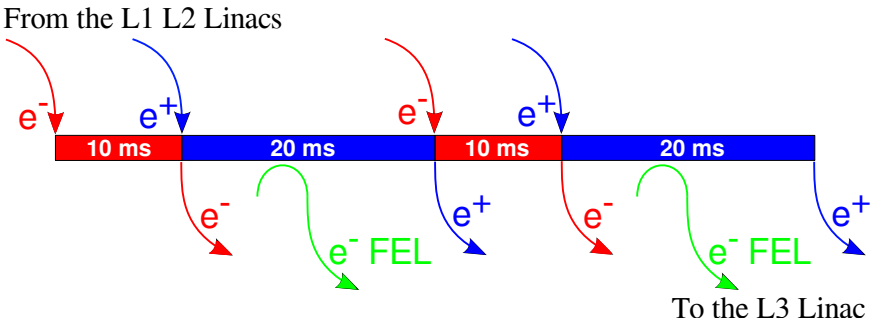

Figure 1.3. *Scheme of two periods of the injection time sequence. The damping ring stores alternately electrons for* 10 ms *and positrons for* 20 ms*. The main Linac works at* 100 Hz *accelerating also the electron beam for the FEL during the damping of the positrons.*

Description

The tight tolerances on the injected beam due to the small acceptance of the collider main rings led to the design of a small emittance, small energy spread and short bunch length Damping Ring which can store alternatively both electrons and positrons at 1 GeV.

Betatron damping times: $\tau_x = 7.26$ ms and $\tau_y = 7.36$ ms [1] ensure adequate reduction of the injected beam emittance and energy spread at the maximum repetition rates of 100 Hz for electrons and 50 Hz for positrons foreseen by the injection scheme, for details of the injection time sequence refer to Fig. 1.3. Tab. 1.1 collects the parameters of the damping ring.

Estimation of the outcome emittances

An upper limit on the bunch size was fixed at $\sigma_x = 5$ mm, so that the 99.7% of the particles are included in $x_{max} = 15$ mm, while the beam stay clear radius is 25 mm. At the same way it was chosen $\sigma_p = 5‰$, so $3\sigma_p \equiv \delta \equiv \Delta p/p_0 = 1.5\%$, well below the RF acceptance at 0.5 MV voltage: 2.5%.

So at the entrance of the damping ring the emittance must be lower than:

$$\varepsilon_i = \frac{\sigma_x^2 - (D\delta)^2}{\beta_x} = 1.1 \ \mu m.$$

Parameter	Unit	Value
Energy	GeV	1.0
Horizontal emittance ε_{0x}	nm	23
Vertical emittance ε_{0y}	nm	0.2
Betatron damping time	ms	7.3
Maximum horizontal beta	m	7.9
Maximum vertical beta	m	7.3
Maximum dispersion	m	0.8
Relative energy spread		6.2×10^{-4}
Momentum compaction		5.7×10^{-3}
RF frequency	MHz	475
RF voltage	MV	0.5
Bunch length	mm	4.8

Table 1.1. *Parameters of the damping ring.*

The emittance of the beams stored in the damping ring varies according to:

$$\varepsilon_{out} = \left[(\varepsilon_{in} - \varepsilon_0)e^{-2t/\tau} + \varepsilon_0\right], \tag{1.1}$$

where ε_0 is the equilibrium emittance, τ is the damping time and t is the storing time.

The parameters of the beams at the exit of the damping ring are collected in Tab. 1.2, these values are the starting point for all the following studies. Note that the emittances of the electron beam are just the equilibrium ones, this is because the electron bunches are produced with low emittance which is not increased by the conversion process.

1.3 OBJECTIVE OF THE WORK

At the exit of the Damping Ring the beams must be accelerated and transported to the Main Rings keeping their emittance and their momentum spread very low in order to satisfy the injection requirements and to minimize the oscillation amplitude of the injected bunches into the rings. This requires an optimization of the parameters of the bunch compressor. Moreover effects of the Coherent Synchrotron radiation and Wake Fields, which are critical in facilities like the LCLS FEL [18] and

Parameter	Symbol	Unit	Electron	Positron
Energy	E	GeV	1.0	1.0
Relativistic factor	γ	-	1957	1957
Horizontal emittance	ε_x	nm	23.0	28.0
Vertical emittance	ε_y	nm	0.2	5.0
Bunch length (RMS)	σ_s	mm	4.8	4.8
Momentum spread (RMS)	δ	‰	0.62	0.62
Horizontal optical function	β_x	m	4.13	4.13
Horizontal optical function	α_x	-	0.258	0.258
Vertical optical function	β_y	m	2.20	2.20
Vertical optical function	α_y	-	0.640	0.640
Number of particles	N_b	-	$1.87 \cdot 10^9$	$1.87 \cdot 10^9$
Total charge	C	pC	−300	300

Table 1.2. *Beams parameters after the Damping Ring.*

the injection system of the Japanese B-Factory SuperKEKB [19], need to be evaluated for the beams of SuperB. Misalignments of the Linac magnets and cavities introduce orbit distortion which lead to increase of the emittance; this must be evaluated and an effective orbit-correction system has to be provided.

2 THEORY

2.1 TRANSPORT

Transport of the particles along a beam line is a central point of this study. In the following the main features of transport theory will be summarized. For further references and detailed derivations refer to [20, 21].

Reference Frame

The motion of particles is described with respect to the reference orbit of the accelerator. This orbit is followed by a particle which enters the line with the design momentum in the centre of the magnetic elements. We can take a reference frame whose origin moves with the reference particle along the accelerator: s axis will point in the direction of motion, the other two axes will be perpendicular. If we assume that the motion lays on an horizontal plane, x axis will point in the horizontal direction orthogonal to s; y axis in the vertical one.

Coordinate System

We need six coordinates to describe the motion of a particle in the 3-D space. Using the *elegant* formalism we can choose the following vector:

$$\vec{X} = \begin{pmatrix} x \\ x' \\ y \\ y' \\ s \\ \delta \end{pmatrix}$$

where x and x' (y and y') describe the horizontal (vertical) displacement with respect to the reference orbit and its derivative, s is the travelled distance and $\delta = \Delta p/p_0$ represents the variation of the momentum with respect to p_0, the reference one.

Each element that the particle encounters going through the beam line acts as a map on the coordinates. At the first order the map can be written as a two dimensional matrix as follows:

$$\vec{X}_f = R_{if}\vec{X}_i$$

where $\vec{X}_i$ and $\vec{X}_f$ are the coordinate vectors at positions s_i and s_f.

The tracking along the beam line is obtained multiplying the matrices of all its n elements:

$$\vec{X}_f = R_{fn}\, R_{n\,n-1}\, \ldots\, R_{32}\, R_{2i}\, \vec{X}_i = R\, \vec{X}_i$$

The 6×6 matrix R is the *transport matrix*, its explicit form being:

$$\begin{pmatrix} x \\ x' \\ y \\ y' \\ s \\ \delta \end{pmatrix}_f = \begin{pmatrix} R_{11} & R_{12} & R_{13} & R_{14} & R_{15} & R_{16} \\ R_{21} & R_{22} & R_{23} & R_{24} & R_{25} & R_{26} \\ R_{31} & R_{32} & R_{33} & R_{34} & R_{35} & R_{36} \\ R_{41} & R_{42} & R_{43} & R_{44} & R_{45} & R_{46} \\ R_{51} & R_{52} & R_{53} & R_{54} & R_{55} & R_{56} \\ R_{61} & R_{62} & R_{63} & R_{64} & R_{65} & R_{66} \end{pmatrix} \begin{pmatrix} x \\ x' \\ y \\ y' \\ s \\ \delta \end{pmatrix}_i$$

In the following we will see how some of the R matrix elements are related with physical observables.

2.1.1 2D Transverse Motion

Consider a machine composed only by horizontal bending magnets and quadrupoles without vertical bending. The normalized strength of the quadrupoles is defined as:

$$k = \frac{1}{B\rho}\frac{dB_y}{dx}$$

where $B\rho = p/e$ is the momentum rigidity and dB_y/dx is the field gradient of the quadrupoles. The dynamics of a particle is then given by the Hill's equation:

$$\boxed{y'' + k(s)\, y = 0} \tag{2.1}$$

for the transverse vertical motion and:

$$\boxed{x'' + \left[\frac{1}{\rho(s)^2} - k(s)\right]\, x = 0} \tag{2.2}$$

for the transverse horizontal one. The minus sign in the vertical case comes from the fact that the focusing quadrupoles in the vertical direction are defocusing in the horizontal one. There is also an extra focusing term which is due to the curvature of the trajectory.

A solution for this equation can be written in the general form:

$$u(s) = \sqrt{\varepsilon}\,\sqrt{\beta(s)}\,\cos(\varphi(s) + \varphi_0) \tag{2.3}$$

where u(s) is either $x(s)$ or $y(s)$. $\sqrt{\varepsilon}$ and φ_0 are integration constants.

Two conditions must be satisfied in order to obtain a solution of the Hill's equation 2.2. The first condition is on the phase function φ:

$$\varphi'(s) = \frac{1}{\beta(s)} \quad \Leftrightarrow \quad \varphi(s) = \int \frac{ds}{\beta(s)} \tag{2.4}$$

The second condition is the differential equation for the function $\beta(s)$:

$$\alpha' = k(s)\beta - \gamma$$

where: $\alpha = -1/2\beta', \quad \gamma = (1+\alpha^2)/\beta, \quad \alpha' = -1/2\beta''$.

The derivative of 2.3 is:

$$u'(s) = \sqrt{\varepsilon}\,\frac{\alpha}{\sqrt{\beta}}\,\cos(\varphi(s) + \varphi_0) - \frac{\sqrt{\varepsilon}}{\beta}\,\sin(\varphi(s) + \varphi_0). \tag{2.5}$$

Eliminating the phase $(\varphi - \varphi_0)$ between u and u' we obtain the constant of motion which is also called Courant Snyder invariant:

$$\gamma u^2 + 2\alpha u u' + \beta u'^2 = \varepsilon \tag{2.6}$$

This invariant expression is the equation of an ellipse with area $\pi\varepsilon$ in the phase space uu'. The parameters of the ellipse α, β, γ and the phase function φ are called betatron functions. The transport matrix $M_{x,y}$ from s_i to s_f can be expressed in terms of the betatron functions α, β, γ and $\mu = \varphi(s_f) - \varphi(s_i)$ as:

$$M = \begin{pmatrix} \sqrt{\dfrac{\beta_f}{\beta_i}}(\cos\mu + \alpha_i \sin\mu) & \sqrt{\beta_i\beta_f}\sin\mu \\ \dfrac{\alpha_i - \alpha_f}{\sqrt{\beta_i\beta_f}}\cos\mu - \dfrac{1+\alpha_i\alpha_f}{\sqrt{\beta_i\beta_f}}\sin\mu & \sqrt{\dfrac{\beta_i}{\beta_f}}(\cos\mu + \alpha_f\sin\mu) \end{pmatrix} \tag{2.7}$$

.

In case of a periodic cell ($\alpha_i = \alpha_f = \alpha$, $\beta_i = \beta_f = \beta$) M reduces to:

$$M_p = \begin{pmatrix} \cos\mu + \alpha\sin\mu & \beta\sin\mu \\ -\gamma\sin\mu & \cos\mu - \alpha\sin\mu \end{pmatrix}. \tag{2.8}$$

With these results we can write:

$$\begin{pmatrix} x \\ x' \\ y \\ y' \\ s \\ \delta \end{pmatrix}_f = \begin{pmatrix} M_x & & R_{13} & R_{14} & R_{15} & R_{16} \\ & & R_{23} & R_{24} & R_{25} & R_{26} \\ R_{31} & R_{32} & & M_y & R_{35} & R_{36} \\ R_{41} & R_{42} & & & R_{45} & R_{46} \\ R_{51} & R_{52} & R_{53} & R_{54} & R_{55} & R_{56} \\ R_{61} & R_{62} & R_{63} & R_{64} & R_{65} & R_{66} \end{pmatrix} \begin{pmatrix} x \\ x' \\ y \\ y' \\ s \\ \delta \end{pmatrix}_i$$

This allows propagating any trajectory trough an arbitrary beam line.

2.1.2 Longitudinal Dynamics and Dispersion

In the bending magnets the deflection of particles with a momentum deviation Δp is different with respect to that of particles with the reference momentum. In linear approximation this is represented by an extra term proportional to $\Delta p/p_0$ in the Hill's equation:

$$x'' + \left[\frac{1}{\rho(s)^2} - k(s)\right] x = \frac{1}{\rho(s)}\frac{\Delta p}{p_0}$$

or, more compactly:

$$\boxed{x'' + K(s)\, x = \frac{\delta}{\rho(s)}} \qquad K(s) \equiv \frac{1}{\rho(s)^2} - k(s); \quad \delta \equiv \frac{\Delta p}{p_0} \tag{2.9}$$

where $\rho(s)$ is the local radius of curvature of the reference trajectory.

Since δ is assumed to be constant, then if x is a solution of equation 2.9 for a given δ, $n \cdot x$ will be a solution for $n \cdot \delta$. Therefore it is useful to normalize x with respect to δ:

$$D(s) \equiv \frac{x}{\delta} = \frac{x}{\Delta p/p_0} \tag{2.10}$$

$D(s)$ is called *Dispersion trajectory* and it describes the momentum-dependent part of motion. It is a particular solution of the following inhomogeneous equation:

$$D''(s) + K(s)\, D(s) = \frac{1}{\rho(s)} \tag{2.11}$$

The dispersion trajectory can be calculated by solving the above equation as described in the references [20, 21]. We call $D(s)$, $D'(s)$ the particular solution with initial conditions $D(s_i) = D'(s_i) = 0$, assuming that particles of different energies have the same initial position as the reference particle. The particle coordinates at position s_f are related to their initial values at s_i by the following linear transformation:

$$\begin{pmatrix} x(s_f) \\ x'(s_f) \end{pmatrix} = M_{fi} \begin{pmatrix} x(s_i) \\ x'(s_i) \end{pmatrix} + \delta \begin{pmatrix} D(s_f) \\ D'(s_f) \end{pmatrix}$$

which can also be written as:

$$\begin{pmatrix} x \\ x' \\ \delta \end{pmatrix}_{s=s_f} = \begin{pmatrix} M_{fi} & \begin{matrix} D \\ D' \end{matrix} \\ \begin{matrix} 0 & 0 \end{matrix} & 1 \end{pmatrix} \begin{pmatrix} x \\ x' \\ \delta \end{pmatrix}_{s=s_i}$$

Only the horizontal dispersion has been considered up to now, however vertical dispersion can be present also in a fully-horizontal machine, coming from alignment errors of the magnets.

Summing up all the previous results, the transport matrix equation becomes:

$$\begin{pmatrix} x \\ x' \\ y \\ y' \\ s \\ \delta \end{pmatrix}_f = \begin{pmatrix} M_x & \begin{matrix} R_{13} & R_{14} & R_{15} & d_x \\ R_{23} & R_{24} & R_{25} & d'_x \end{matrix} \\ \begin{matrix} R_{31} & R_{32} \\ R_{41} & R_{42} \end{matrix} & \begin{matrix} M_y & \begin{matrix} R_{35} & d_y \\ R_{45} & d'_y \end{matrix} \end{matrix} \\ \begin{matrix} R_{51} & R_{52} & R_{53} & R_{54} & R_{55} & R_{56} \\ 0 & 0 & 0 & 0 & R_{65} & 1 \end{matrix} \end{pmatrix} \begin{pmatrix} x \\ x' \\ y \\ y' \\ s \\ \delta \end{pmatrix}_i \tag{2.12}$$

2.1.3 Beam Envelopes

Most of the elements which can be found on a line are represented by unitary matrices, this ensures a symplectic tracking in which the Poisson bracket is preserved and the Liouville's theorem can be applied. This means that even if the phase space of the beam can be stretched and rotated by various kinds of magnets, the area is generally kept constant[1]. A common way to refer to this area is by the emittance ε for which the relation $A = \pi\varepsilon$ subsists, where the area A encloses one σ of a Gaussian beam distribution.

1 This is not valid for instance for accelerating cavities in which adiabatic damping of the emittance take place

Given the emittance, the transverse sizes of the beam are determined from the values of the optical functions as follows:

$$\sigma_x = \sqrt{\varepsilon\beta + \left(D(s)\delta\right)^2} \tag{2.13}$$

$$\sigma_{x'} = \sqrt{\varepsilon\gamma} = \sqrt{\varepsilon\frac{1+\alpha^2}{\beta}} \tag{2.14}$$

2.1.4 Momentum Compaction Factor - R_{56}

Momentum values different from the reference one will lead the particle to travel on the dispersion trajectory. All the particles considered are ultra-relativistic so they share the same velocity $\approx c$, but if the length of the reference and the dispersion trajectory are different, particles with different momentums will travel the line in different times being pushed in the longitudinal direction.

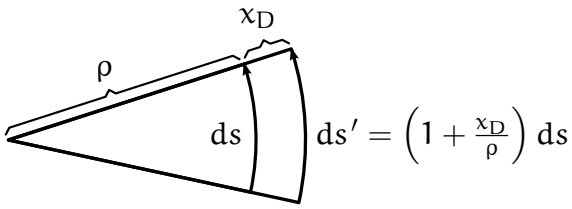

The length of the path of the dispersion trajectory is:

$$\begin{aligned} L' &= \int_{s_1}^{s_2} ds' = \int_{s_1}^{s_2} \left(1 + \frac{x_D(s)}{\rho}\right) ds \\ &= \int_{s_1}^{s_2} ds + \int_{s_1}^{s_2} \frac{x_D(s)}{\rho} ds = L_0 + \Delta L \end{aligned}$$

and introducing the proportional relation:

$$\frac{\Delta L}{L_0} = \alpha(s_1, s_2)\frac{\Delta p}{p_0} \tag{2.15}$$

we finally get the expression of the momentum compaction factor:

$$\boxed{\alpha(s_1, s_2) = \frac{1}{L_0}\int_{s_1}^{s_2} \frac{D(s)}{\rho(s)} ds} \tag{2.16}$$

which has been simplified using the definition of the dispersion 2.10.

Now we shall see how the momentum compaction factor is related to the entries of the transport matrix.

We can start from the matrix equation:

$$\begin{pmatrix} s_2 \\ \delta_2 \end{pmatrix} = \begin{pmatrix} R_{55} & R_{56} \\ R_{65} & R_{66} \end{pmatrix} \begin{pmatrix} s_1 \\ \delta_1 \end{pmatrix} = \begin{pmatrix} R_{55}s_1 + R_{56}\delta_1 \\ R_{65}s_1 + R_{66}\delta_1 \end{pmatrix}$$

and we consider the first line:

$$s_2' = R_{55}s_1 + R_{56}\delta_1 = s_2 + R_{56}\delta_1 \tag{2.17}$$

In this equation we stressed the fact that if δ_1 is zero, namely the momentum of the particle at the beginning of the line is the reference one, the particle will follow the ordinary trajectory to the s_2 position. Otherwise, if a momentum spread is present, the particle will follow the dispersion trajectory to the s_2' position.

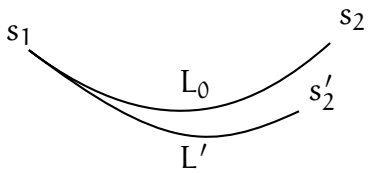

Let us compute:

$$\begin{aligned} \Delta L =& L' - L_0 = \int_{s_1}^{s_2'} ds - \int_{s_1}^{s_2} ds = \int_{s_1}^{s_2'} ds + \int_{s_2}^{s_1} ds \\ \approx & \int_{s_2}^{s_2'} ds \approx s_2' - s_2 \end{aligned}$$

The approximation is valid in case of small paths. We now can rewrite the proportionality relation 2.15 as follows:

$$\frac{s_2' - s_2}{L_0} \approx \alpha(s_1, s_2)\delta_1 \tag{2.18}$$

substituting s_2' with the result of equation 2.17 we obtain:

$$\begin{aligned} \frac{R_{55}s_1 + R_{56}\delta_1 - s_2}{L_0} \approx & \alpha(s_1, s_2)\delta_1 \\ \frac{s_2 + R_{56}\delta_1 - s_2}{L_0} \approx & \alpha(s_1, s_2)\delta_1 \end{aligned}$$

and simplifying:

$$\boxed{R_{56} \approx L_0\, \alpha(s_1, s_2) = \int_{s_1}^{s_2} \frac{D(s)}{\rho(s)}\, ds} \tag{2.19}$$

For a chicane made up of four quadrupoles, like the one presented in Fig. 3.2, the R_{56} can be estimated with the following formula [18]:

$$R_{56} \approx -2\alpha^2 \left(L_1 + \frac{2}{3} L_D \right) \tag{2.20}$$

Referring to the Fig. 3.2, α is the deviation angle of the chicane, L_1 is the distance between the first and the second dipole (equal to the one between the third and the last) and L_D is the length of the dipoles.

2.1.5 R_{65}, R_{55} and second order Transport

R_{65} and R_{55} are very important parameters when considering how a complex line acts on the beam longitudinal shape.

R_{65} tells how much the momentum is changed due to the longitudinal displacement of the particles in a bunch. This parameter is strongly affected by the off-crest-operating RF cavities.

R_{55} indicates how the final longitudinal position is related to the entry one. The values that this parameter assumes, are deeply related to R_{56} and R_{65}. This is exploited in bunch compressors where a zero-crossing cavity provides the R_{65} while the R_{56} comes from the chicane.

However to compute and understand complex lattices the linear dynamics is often inadequate, as many effects require a second order transport to be described. This is often done providing T: a three dimensional tensor; it acts on the coordinates in the following way:

$$X_i = T_i^{jk} X_j X_k \tag{2.21}$$

where index notation has been used with Einstein summation convention.

The second order momentum compaction, namely T_5^{66}, in chicanes without quadrupoles is related to R_{56} by [18]:

$$T_5^{66} \approx -\frac{3}{2} R_{56} \tag{2.22}$$

In [22] many transport matrices are presented for the most common elements.

2.2 SYNCHROTRON RADIATION

2.2.1 Brief history

The fact that accelerated charges emit energy under the form of electromagnetic waves is well know as a direct implication of Maxwell's equations. This phenomena has been used in many fields for example in telecommunications since the end of the 19^{th} century. High energy radiation was observed for the first time at a betatron during the forties at the 70 MeV Synchrotron at General Electric; before of this, the only sources of high energy radiation had been Crookes tubes.

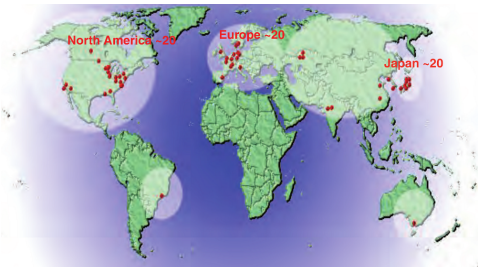

Synchrotron radiation facilities around the world.

The availability of high energy (UV and X-rays) monochromatic radiation is of extreme interest for matter physics, chemistry and biology as it allows to determine the chemical composition and the internal architecture of cells and other biological structures, it opens fabrication techniques, permits the identification of the provenance of archaeological artefacts and many others applications. In the last fifty years many dedicated machines were studied and built to provide high luminosity light sources. At the moment new technologies like Free Electron Lasers are quickly improving and a new generation of light sources covering a wide part of the UV and X-ray spectrum region, will be soon ready.

2.2.2 Emission of Synchrotron Radiation

In this section the main features of synchrotron radiation will be shortly presented. For a detailed derivation and more material please refer to [23, 24, 25].

The opening angle

Consider an ultra-relativistic electron whose path is bent in a dipole. In the inertial reference frame passing through the centre of the dipole

with the same velocity of the electron, its trajectory will be a cycloid with a cusp at the origin. In this reference frame the electron emits like an Hertz dipole as shown in Fig. 2.1.

To obtain the radiation which is seen in the laboratory, a Lorentz boost has to be applied. The result is that all the radiation is contained in a small cone which spreads in front of the particle as shown in Fig. 2.2. The aperture of this cone is:

$$\sin\frac{\theta}{2} = \frac{1}{\gamma} \quad \Rightarrow \quad \theta \approx \frac{2}{\gamma}\,, \quad \gamma \gg 1 \tag{2.23}$$

where γ is the Lorentz factor: $\gamma = E/E_0 = 1/\sqrt{1-\beta^2}$, $\beta = v/c$.

The energy spectrum

The typical wavelength emitted in long dipoles can be estimated considering the time interval in which an observer is exposed to the radiation cone. For an ultra-relativistic particle this time can be written as:

$$\Delta t = \frac{4R}{3c\gamma}$$

from this it is possible to get the frequency and the wavelength:

$$\boxed{f = \frac{3c\gamma}{4R}} \qquad \boxed{\lambda = \frac{4R}{3\gamma^3}}\,. \tag{2.24}$$

The derivation of the spectral distribution is beyond the scope of this study, if interested please refer to [23]; however some spectra are presented in Fig. 2.3 where the newest operating machines are compared to the light which may be obtained from the rings of SuperB. Note that these spectra comes from particular magnets called undulators and the formula 2.24 does not predict the typical frequency of these short magnets, however the shape of the spectra is quite similar.

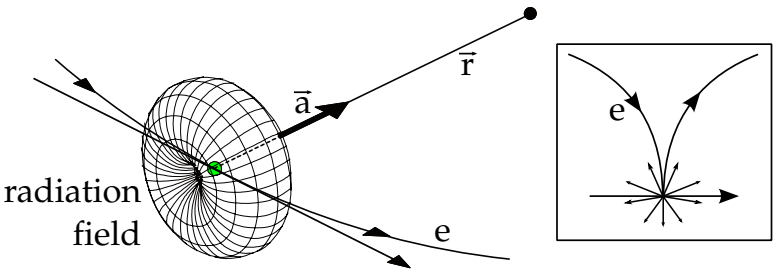

Figure 2.1. *Schematics of the radiation emitted in the moving frame of reference.*

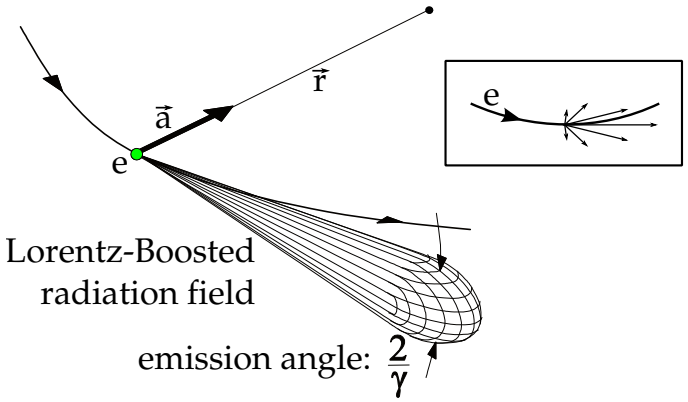

Figure 2.2. *Radiation field boosted in the laboratory frame.*

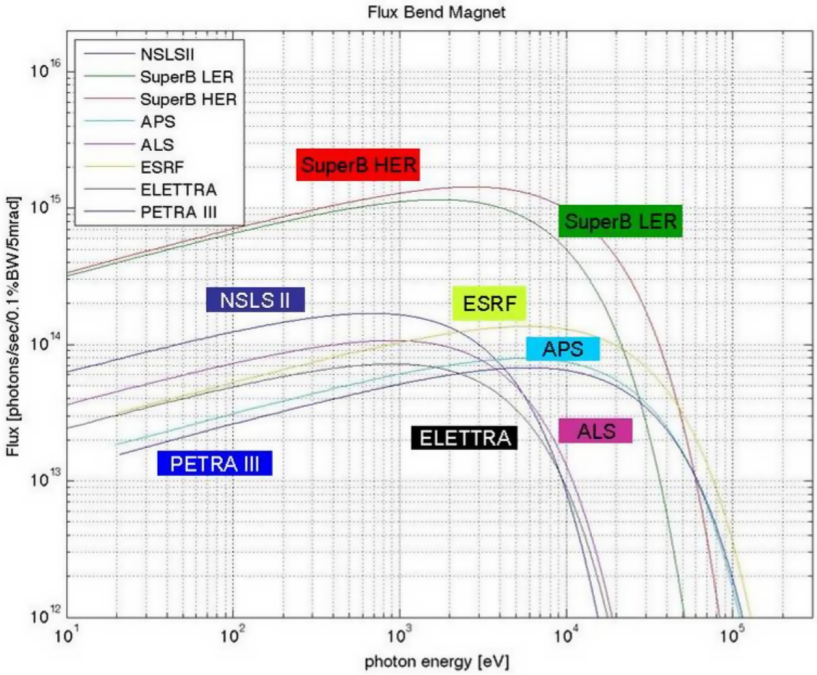

Figure 2.3. *Synchrotron radiation spectra obtainable from the main rings of SuperB compared to the newest operating light source machines.*

2.2.3 Coherent Synchrotron Radiation

Up to now only single particle radiation has been considered, but in the last decades the particle density in the bunches has reached higher and higher values and collective effects spread out.

One of the firsts articles focusing on the coherent radiation (CSR) in electron storage ring was written in 1982 by F. Curtis Michel [26]. He

noted that for wavelength of emission longer than the bunch size, the whole bunch acts as a single particle of charge equal to $N_b\, e$ where e is the electron charge and N_b is the number of electrons stored, typically $N_b \sim 10^{10}$.

The ratio between the power emitted by coherent and incoherent radiation as computed in [23] turns out to be:

$$\frac{P_{coh}}{P_{incoh}} = 0.5257 \frac{N_b}{\gamma^4 (\sigma_s/R)^{4/3}} \tag{2.25}$$

The shielding effect of the beam pipe has not been considered here. The propagation of waves whose length is comparable with the size of the vacuum chamber is inhibited. It often happens that due to the geometry of the chamber the suppression occurs at wavelength shorter than the one which could be radiated coherently. However in linear accelerators bunches short enough to produce coherent emission have been achieved and bursts of infra red coherent radiation have been seen also in storage rings triggered by beam instabilities [23].

A qualitative spectrum taking into account the coherent radiation is presented in Fig. 2.4.

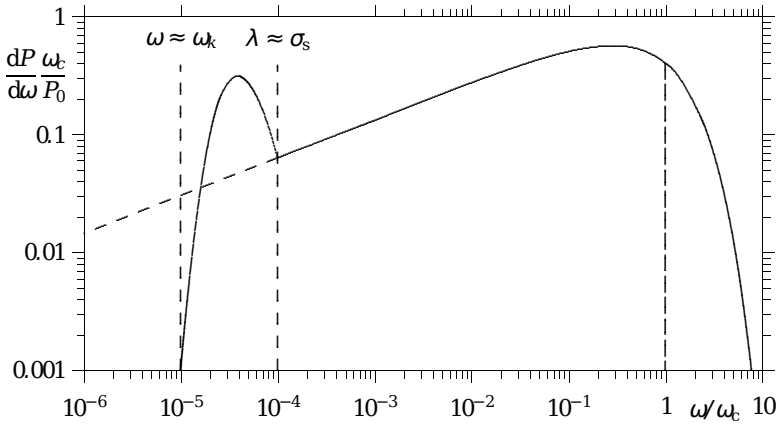

Figure 2.4. *A qualitative spectrum taking count of the coherent radiation.*

Wavelengths shorter than the bunch length generally behave as incoherent even if longer than the distance between the particles. This is due to the quantum excitation that smears out any constructive interference.

2.2.4 Wavelength similar to the Bunch Length

The case of $\lambda \approx \sigma_s$ is particular and must be treated carefully, this has been done with the help of [27]. The assumption that the typical wavelength of incoherent radiation (see Eq. 2.24) is much shorter than the bunch size is made here. In the region $\lambda \approx \sigma_s$ the radiation is coherent in parts of the bunch, so the effects that it produces depend on the charge distribution in the bunch. An interaction between the coherent radiation emitted by a part of the bunch and another part of it may produce differences in the energy losses along the bunch.

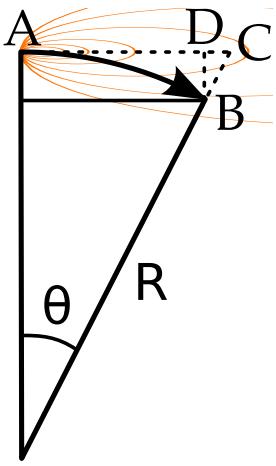

Consider a beam bent in a dipole. The particles and the emitted radiation have nearly same velocity: c, but while the particles follow a curved trajectory, the radiation travels in straight line. The radiation emitted by the tails of the bunch may reach the head of the bunch. Calling s a distance of the order of the bunch length, the condition for this to happen is:

$$\begin{aligned} s &= \overset{\frown}{AB} - \overline{AB} = R\theta - 2R\sin(\theta/2) \\ &\approx \frac{1}{24}\theta^3 R, \qquad \theta \ll 1 \end{aligned} \tag{2.26}$$

Other geometrical relations can be derived:

$$\theta = 2\sqrt[3]{\frac{3s}{R}}, \quad L_0 = \overline{AB} = 2\sqrt[3]{3sR^2}, \quad r = \overline{DB} = L_0\theta/2 = 2\sqrt[3]{9s^2R} \tag{2.27}$$

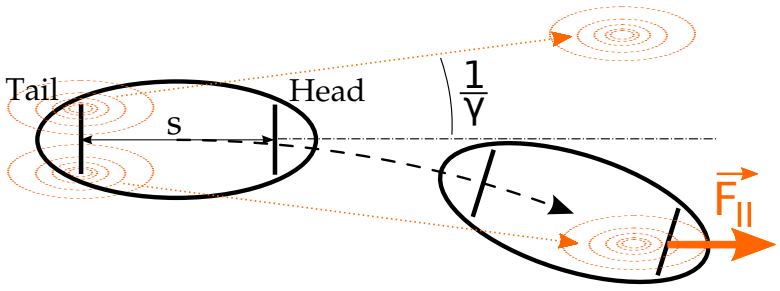

Figure 2.5. *Schematic representation of the bunch tail-head interaction generating a longitudinal force.*

To approach the problem the bunch has been represented as shown in Fig. 2.5. The electric field emitted by the tail of the bunch is approximated with the field of a straight charged wire:

$$E_\perp \approx \frac{2N_b e\lambda}{r} \tag{2.28}$$

where λ here represents the linear charge density; for simplicity it can be considered constant, so its value is the inverse of the length of the bunch: $\lambda = 1/\sigma_s$.

The characteristic longitudinal force can now be written as:

$$F_\parallel = eE_\perp \cdot \theta = \frac{2N_b e^2\lambda\theta}{r} = \frac{2N_b e^2\lambda}{\sqrt[3]{3sR^2}} \tag{2.29}$$

This force leads to a redistribution of the energy inside the bunch. The head collects some of the energy radiated by the tail. However the total energy change is negative. In addition to the longitudinal force $F_\parallel$, also transverse forces take place, but they are attenuated of a factor θ and will not be treated here.

A couple of geometric constraints should still be considered:

1. A short dipole which does not allow the complete overtake of the bunch by the radiation.

2. A small beam pipe which prevents the radiation from travelling a straight line to the head of the bunch.

Short Dipole

In this case only a fraction of the bunch produces radiation that can reach the head and a smaller portion of the particles contributes: $N_{eff} = N_b\ s_{eff}/\sigma_s$. The length of the dipole $L_d < L_0$ and the curvature radius R determine the difference between the arc and the straight line path. The expression of s_{eff} can then be derived similarly as Eq. 2.27:

$$s_{eff} \approx \frac{L_d^3}{24R^2} \tag{2.30}$$

Note from Eq. 2.29 that the longitudinal force scales with $s^{-1/3}$ while N scales with s, so altogether:

$$F_\parallel \sim F_\parallel\Big|_{L_d \geqslant L_0} (s_{eff})^{2/3} = F_\parallel\Big|_{L_d \geqslant L_0} \left(\frac{L_d^3}{24\sigma_s R^2}\right)^{2/3} \propto L_d^2 \tag{2.31}$$

Small Beam Pipe

If the beam pipe radius is not large enough, the radiation produced by the particles in the tail is shielded by the chamber and can not reach the head of the bunch. Calling h the pipe height, the shielding happens for: $h < r/2$ where r is defined in Eq. 2.27. In this case $s_{eff} = \sqrt{h^3/(8R)}$ and the force scales as:

$$F_{\parallel} \sim F_{\parallel}\Big|_{h \geqslant r/2} \left(\frac{1}{\sigma_s}\sqrt{\frac{L_d^3}{R}}\right)^{2/3} \propto L_d \tag{2.32}$$

Fig. 2.6 from [18] shows the typical effects of the CSR for a shielded and unshielded bunch, $h_c \equiv \sqrt[3]{\pi^2\sigma_s^2 R}$: the height for which $s_{eff} \approx s$ has been introduced there.

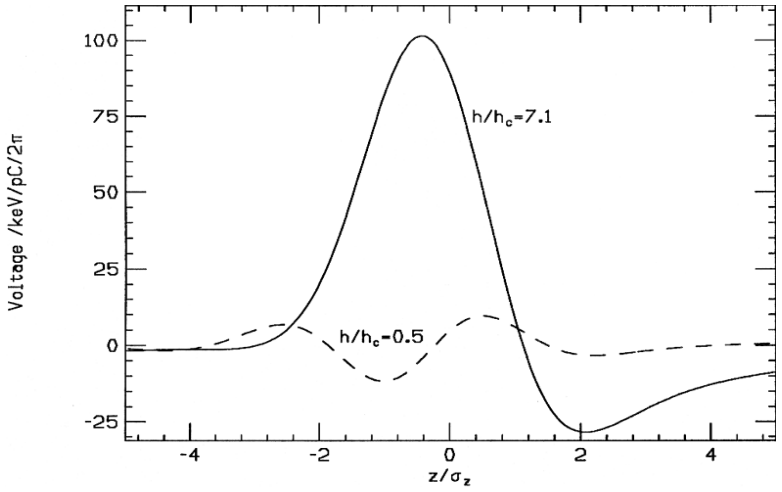

Figure 2.6. *Coherent radiation steady-state wake per 2π bend ($R = 19.4$ m, $\sigma_s = 30$ μm, $h_c = 5.6$ mm) for both shielded (dash: $h/h_c = 0.5$) and unshielded (solid: $h/h_c >> 1$) coherent radiation of a gaussian bunch. Here the bunch head is at $z > 0$ and $V > 0$ represents energy loss.*

2.2.5 Fast estimation of the CSR effects

The following formula allows a fast estimation of the momentum spread induced by CSR in a bunch whose charge has a longitudinal Gaussian distribution [27]:

$$\Delta p/p \approx 0.22\,\frac{N_b r_e L_d}{\gamma\sqrt[3]{\sigma_s^4 R^2}} \tag{2.33}$$

here the numerical coefficient comes from the Gaussian shape and $r_e = 2.818 \cdot 10^{-15}$ m is the electron classical radius.

The emittance growth is given by [18]:

$$\frac{\varepsilon}{\varepsilon_0} \approx \sqrt{1 + \frac{0.22^2}{36} \frac{r_e^2 N_b^2}{\gamma^2 \varepsilon_0 \beta} \left(\frac{|\theta|^5 L_d}{\sigma_s^4} \right)^{2/3} \left[L_d^2 (1 + \alpha^2) + 9\beta^2 + 6\alpha\beta L_d \right]}, \tag{2.34}$$

the optical functions α and β have been introduced here. This formula is typically applied to the last magnet of a chicane which gives the highest CSR effects, so it underestimates the total increase of emittance.

Note that what has been afforded up to now is the steady-state of the CSR. Transient effects at the entrance and at the exit of the bending dipoles can be very important. *elegant* takes care of these through the methods described in [28]. Note also that *elegant* only tracks the longitudinal forces and ignores any transverse distribution of the bunch.

2.3 WAKE FIELDS

If the CSR influences the beam dynamics with fields that are generated in the tail of the bunch and reach its head, wake fields do the opposite: fields generated by the head of the bunch get reflected by the walls and affect the tail as sketched in Fig. 2.7. Their effect is particularly evident for low-emittance-short bunches travelling in Linacs where the accelerating fields induce the emission of radiation. Wake fields trigger energy losses in the bunch, increase the momentum spread and consequently reduce the adiabatic damping of the emittance, especially in dispersive areas.

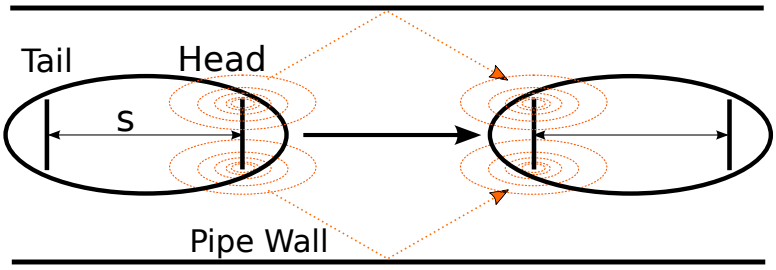

Figure 2.7. *Schematic representation of the wake fields radiation. It is generated by the head of the bunch, get reflected by the wall and interact in the tail.*

2.3.1 Potential and Green Functions

Wake fields computations often start from the Green's function $G(s)$ which describes the field generated by a point-like charge moving across the accelerator structures. Due to the complexity of the geometry, $G(s)$ is generally obtained fitting an analytical function on the data coming from numerical simulations, Fig. 2.8 shows the Green's function used in the SuperB computations. Once $G(s)$ is known the wake field potential of the bunch charge distribution is obtained by the convolution:

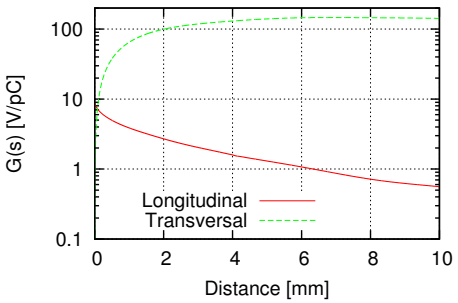

Figure 2.8. *Green's functions used in the SuperB simulations.*

$$W(s) = \frac{1}{Q}\int_{-\infty}^{s} G(s-s')q(s')\,ds' \tag{2.35}$$

where Q is the total charge of the bunch:

$$Q = \int_{-\infty}^{+\infty} q(s)\,ds \tag{2.36}$$

The total energy lost by the bunch is then represented by the loss factor:

$$k = \frac{1}{Q}\int_{-\infty}^{+\infty} W(s)q(s)\,ds \tag{2.37}$$

Typical values for the above physical quantities are plotted in Fig. 2.9 taken from [29].

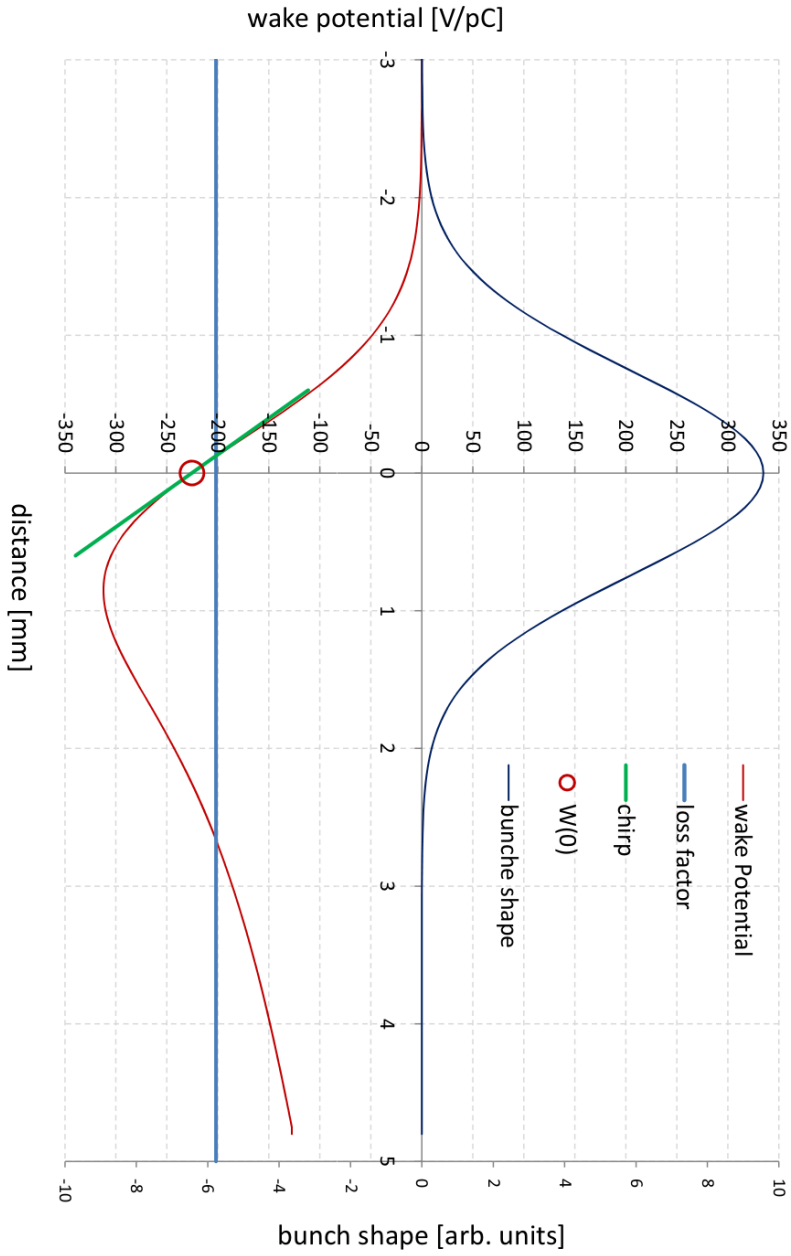

Figure 2.9. *Wake potential of the SLAC accelerating section (the same of SuperB) and bunch shape of a 0.7 mm bunch. The blue line shows the loss factor, which is equal to the averaged value. The red circle and a green line show the value of the wake potential and its derivative (chirp) at the centre of a bunch.*

3 BUNCH COMPRESSOR

3.1 INTRODUCTION

During acceleration only the reference particle on the crest of the RF accelerating field gains the maximum energy, all the other particles in a bunch will be less accelerated according to their phase with respect to the RF voltage. It is therefore important to reduce the phase extension of the bunch (i.e. the longitudinal length), allowing the bunch to be accelerated containing the absolute energy spread and reducing the relative momentum spread to values acceptable for the injection in the main rings. For this purpose, the injector of SuperB includes a bunch compressor system placed in the transfer lines connecting the damping ring (DR) to the high energy Linac.

The bunch compressor consists of a RF cavity followed by a chicane made up with at least three dipoles, see Fig. 3.1. The RF section accelerates the bunches with an off-crest RF phase, thereby introducing a correlated energy spread along them. Particles in the bunch tail acquire a higher energy than those in the head. Bunches travel then the chicane, whose path length depends on the particle energy. The trajectory of tail-higher-energy particles across the chicane is shorter than the one of the head-low-energy particles. Since all of them have the same velocity $\approx c$, the tail particles travel the chicane in less time than the reference particle, while the head particles need more time, so both are driven to the centre of the bunch. This process keeps constant the area of the phase space, consequently the price to pay for a compression is the increase of the momentum spread which comes from the RF cavity. However, during the acceleration in the Linac, adiabatic damping take place and the momentum spread is reduced proportionally to the ratio between the initial and the final energy.

The relative energy spread at the end of the Linac depends on the phase extension of the bunch and on the energy spread introduced by the compressor cavity. The bunch compressor parameters have been optimized to minimize the momentum spread at the exit of the Linac.

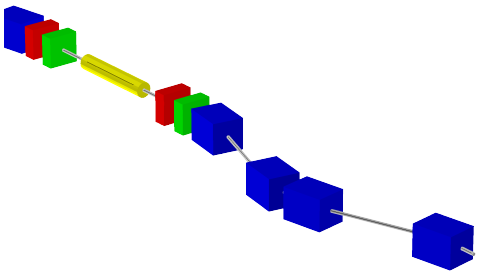

Figure 3.1. *View of the bunch compressor. The yellow cylindrical item is the RF cavity (3 m long). The dipoles are blue. Green and red objects are quadrupoles.*

A previous study of the bunch compressor for SuperB was made by Antoine Chanché. He optimized the system minimizing the momentum spread at the end of the Linac using an analytical approach. He also explored the feasibility of a multiple chicane system to reduce non linearities, but he concluded that such a layout would not bring an important improvement [2].

After the institution of the Cabibbo Lab at Tor Vergata, which will host the SuperB B-Factory, the layout of the injector system has been modified to better fit the new site configuration. A multiple-chicanes scheme would hardly fit into the available longitudinal space. The single-chicane scheme has been re-designed and optimized taking into account beam dynamics effects as coherent synchrotron radiation in the chicane and wake fields in the Linac. Also the possibility to use an L-band cavity, as the ones proposed for the positrons source system, has been investigated. The optimization criteria is still minimization of the momentum spread at the end of the Linac which is a critical parameter for the injection. Chap. 5 presents a detailed description of the optimization.

3.2 DESIGN

The entire beam line from the damping ring to the end of the Linac has been implemented in *elegant* [4] for both electron and positron beams. The transfer lines used to transport the beam parameters from the damping ring to the compressor [3] have been updated.

Many are the parameters which influence the behaviour of the bunch compressor, such as the frequency, voltage and phase of the cavity and

the geometry of the chicane. In Fig. 3.2 a scheme of the chicane is presented. Actually it is a double chicane, which operates on both electron and positron beams. The first and the last magnets act as beam splitter and combiner.

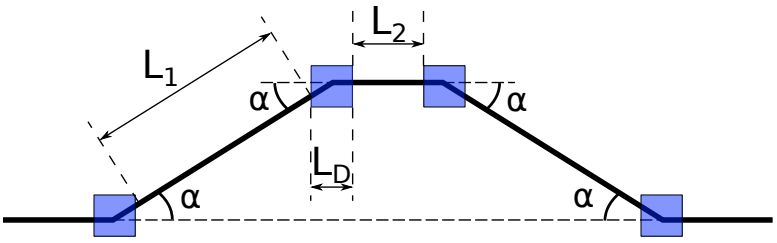

Figure 3.2. *Scheme of the geometric parameters of the chicane. The blue squares represent the dipoles.*

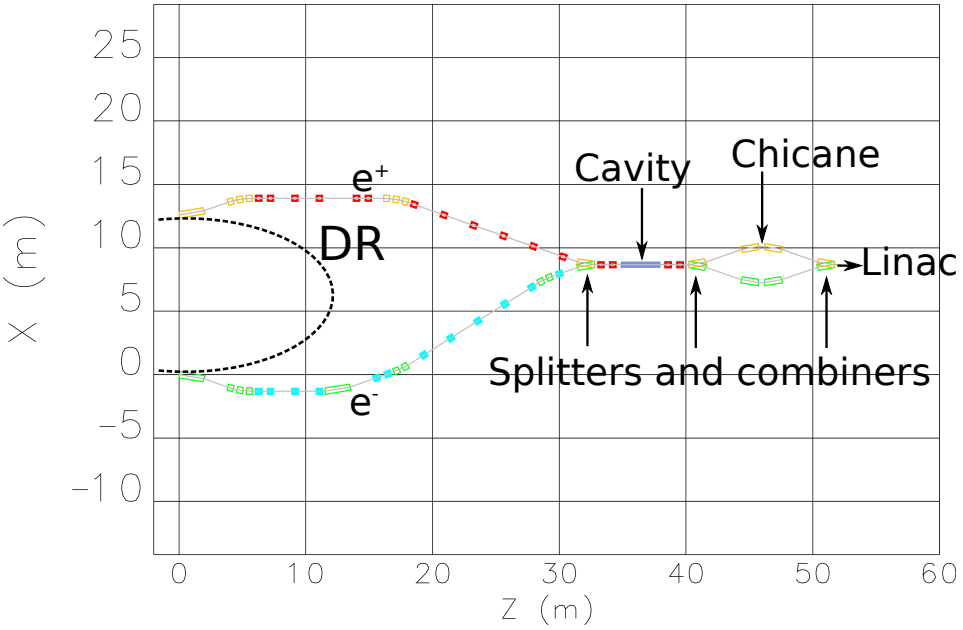

Figure 3.3. *Lattices of the electrons and positrons transfer line from the Damping Ring to the Linac with the new layout of the bunch compressor.*

A particular care has been taken in order to contain the total length of the bunch compressor. An advantage comes from the choice of using dedicated magnets instead of recycling the PEPII magnets as was previously foreseen; this allows to use one long magnet in place of a group of three short ones, saving some space. The new magnets keep the same

field intensity (working point at 0.83 T) and acceptance (35 mm) of the old ones, so the α angle can not be pushed much above 20°. The L_1 minimum distance is then fixed at 3 m to provide ~ 2 m of separation between the two branches of the chicane. The distance L_2, needed for the diagnostic, has been reduced from 1 m to 0.5 m. The tuning of the parameters of the bunch compressor is discussed in Chap. 5. The full layout of the new design of the compressor with the transfer lines from the damping ring is presented in Fig. 3.3. The total length of the bunch compressor has been reduced of about 3 m.

3.3 CHARACTERIZATION

The optical functions and the beam envelopes from the damping ring to the end of the compressor are presented in Fig. 3.4, Fig. 3.5 and Fig. 3.6. In particular note in Fig. 3.5 how R_{56} grows up in the middle of the transfer line. This is due to the dipoles placed at high-dispersion locations. The longitudinal distribution of the beam is nearly unaffected by this because s and δ are uncorrelated before the RF cavity.

The optical functions are different with respect to the ones in [3] because the focusing effect of the cavity was introduced. Moreover the length of the cavity was raised from 1 m to 2.97 m, becoming equal to the ones used in the main Linac.

The optimization of the lines was done independently, so a rematch will be required for the final design in order to let them share the few common magnets. Doing this, the final values the optical function could be raised closer to 50 m, so it would also be easier to match them to the Linac.

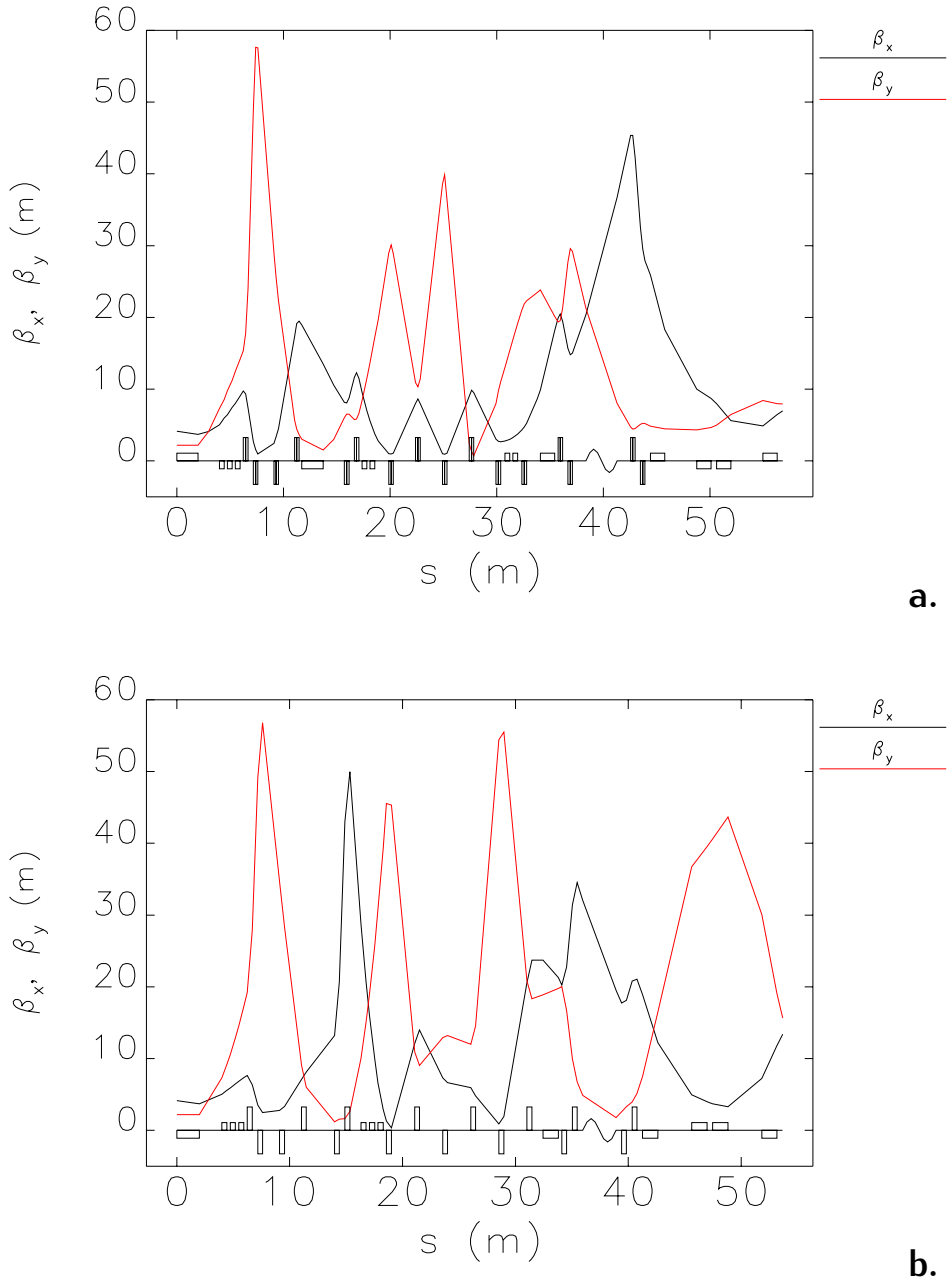

Figure 3.4. *Transverse optical functions of the electrons (a.) and the positrons (b.) transfer lines.*

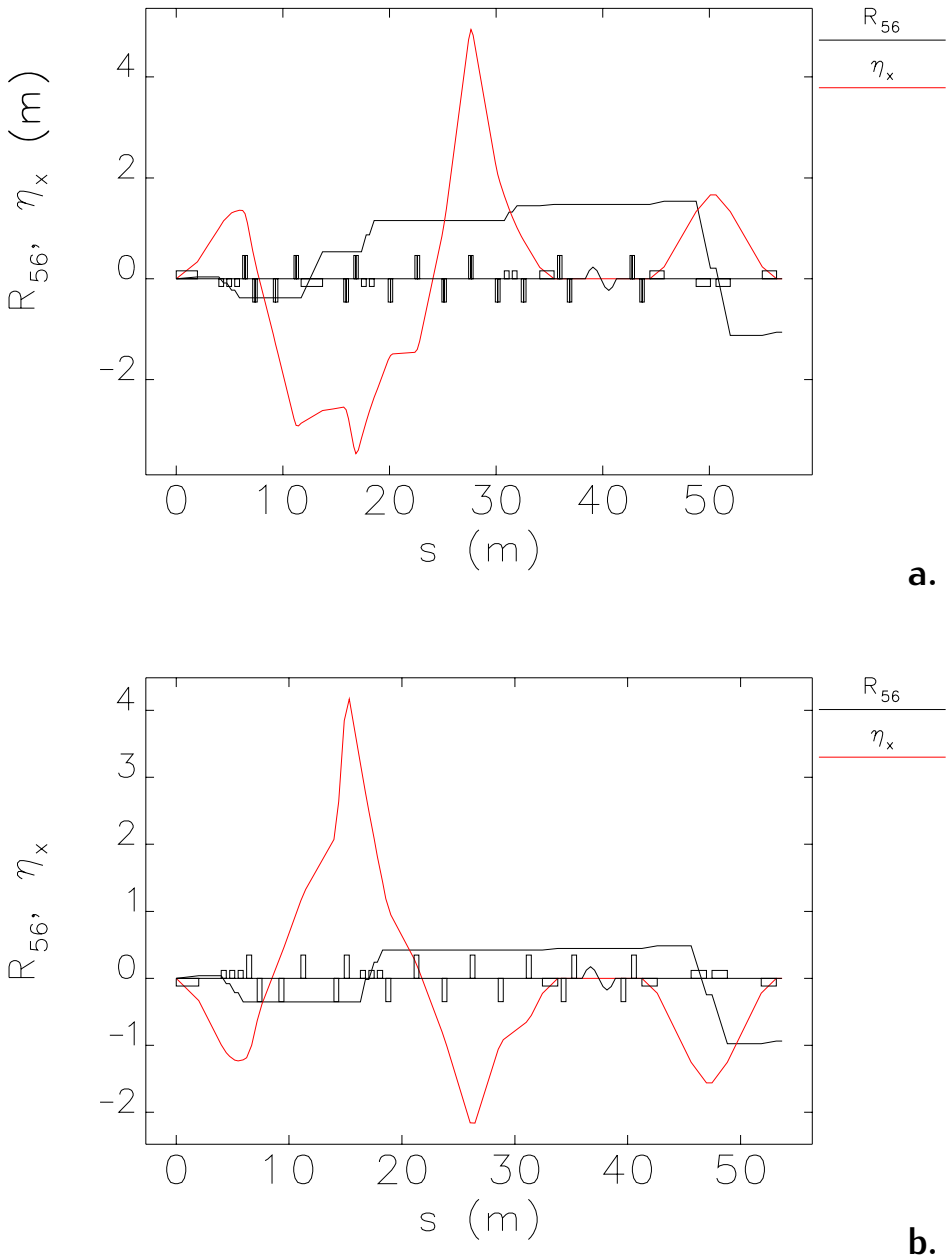

Figure 3.5. *Horizontal dispersion (η_x) and R_{56} computed along the electrons (a.) and the positrons (b.) transfer lines.*

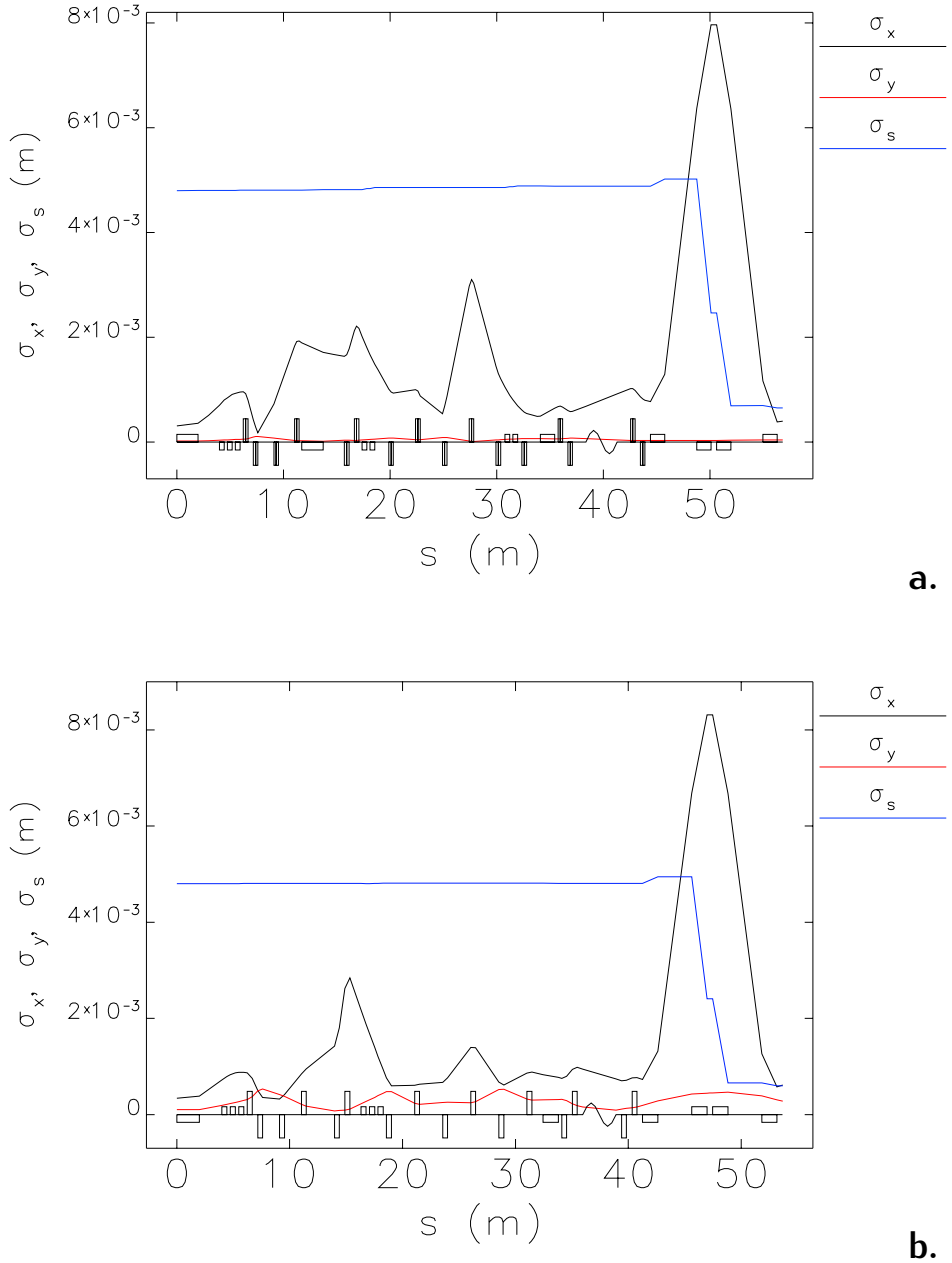

Figure 3.6. *Beam envelopes of electrons (a.) and positrons (b.) tracked along the transfer lines.*

3.4 COHERENT SYNCHROTRON RADIATION EFFECTS

For a theoretical introduction, please refer to Sec. 2.2. The effects of the Coherent Synchrotron Radiation (CSR) on the SuperB bunches can be estimated through Eq. 2.33 using the data reported in Tab. 1.1 ($N_b = 1.87 \cdot 10^9$, $\sigma_s = 4.8$ mm) and in Tab. 5.3 ($L_d = 1.35$ m, $R = 4.07$ m). The result is:

$$\Delta p/p = 0.22 \frac{N_b r_e L_d}{\gamma \sqrt[3]{\sigma_s^4 R^2}} \approx 3.87 \cdot 10^{-7} \tag{3.1}$$

which is several orders of magnitude below the momentum spread of the bunches of SuperB.

However, to take into account all the possible effects contributing to the beam distribution, also the CSR has been considered in the numerical simulation. Using *elegant*, the CSR has been implemented in the dipoles of the chicane and in the drift spaces between them. Fig. 3.7 shows the CSR-induced momentum spread and the beam profile in the last magnet of the chicane, where the bunch is shorter and the effects are more evident. Successive plots refer to successive sections of the magnet. In the firsts two it is possible to note that the potential is rising in the transient region, the central plots show the transition to the steady-state which is reached at the end of the dipole. The energy change computed is of the same order of the one predicted by Eq. 3.1 with $p = 1.0$ GeV/c.

The present design of the injector uses bunches of low charge and not much compressed in the longitudinal dimension compared to a similar project like SuperKEKB [30], see Tab. 3.1. This allows SuperB to avoid the momentum spread and emittance increase induced by the CSR. Also the longitudinal profile of the bunch is not appreciably altered.

	SuperB	SuperKEKB
Bunch Charge (nC)	0.3	5.0
Bunch Length (mm)	$\sigma = 4.8$ (Gaussian)	3.0 (Uniform)

Table 3.1. *Comparison of the CSR relevant parameters between SuperB and SuperKEKB injectors.*

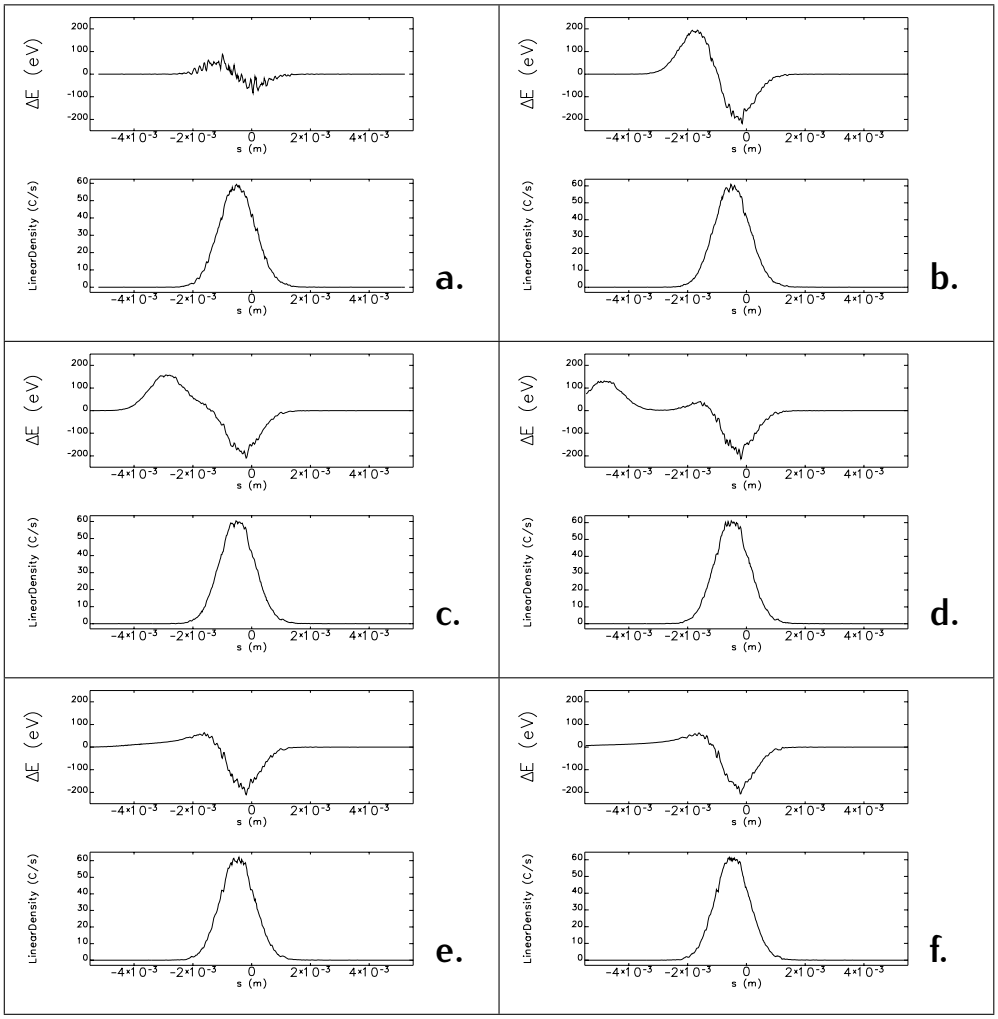

Figure 3.7. *CSR-induced momentum variation and beam profile for successive displacements in the last dipole of the chicane. a,b: at the beginning of the dipole the CSR effects are rising in the transition regime. c,d: in the middle of the dipole part of the impulse travels ahead the bunch. e,f: at the end of the dipole the steady-state is reached.*

4 LINAC

4.1 INTRODUCTION

Linac (LINear ACcelerator) machines are made up of a straight sequence of radio frequency cavities powered by a klystron or a magnetron. Quadrupoles, arranged in focusing-defocusing (FODO) cells, keep the particles focused along the Linac.

With respect to circular machines, Linacs can reach higher energies, because they do not suffer of synchrotron radiation emission; and, regarding the TeV, scale also higher intensities, as the beams do not need to be recirculated and ramped. In order to achieve higher luminosity and higher energy in electron positron colliders, Linacs are taking their way over circular machines, which dominated the landscape of the last fifty years.

4.2 DESIGN

The main Linac of SuperB is composed by 82 radio frequency (RF) cavities. The cavities are travelling wave, constant gradient, $2\pi/3$, 3 m long, 2.856 GHz units operating at a medium gradient of 23.5 MV/m. Each of them is made of a series of 86 RF copper cells, joint with a brazing process, performed in high temperature, under vacuum furnaces [1].

A previous work on the lattice of the Linac was done by Pascal Dominik Hermes [31]. He studied the FODO structure of the Linac, proposing a lattice and simulating its main features. This lattice has been updated and implemented in *elegant*. Four quadrupoles were added at the beginning in order to match the optical functions at the end of the chicane. With the present values of the optical functions, the length of the matching section is between 15 and 18 m. The basic cell of the Linac is sketched in Fig. 4.1. Two cavities are placed between a focusing and the following defocusing quadrupole. λ represents the spatial length of

a cavity period. As the spaces between the cavities are multiples of λ all of them can share the same phase.

In Fig. 4.2 the optical functions of the Linac are presented. At the beginning of the line some space is taken by the four quadrupoles needed to match the output of the bunch compressor.

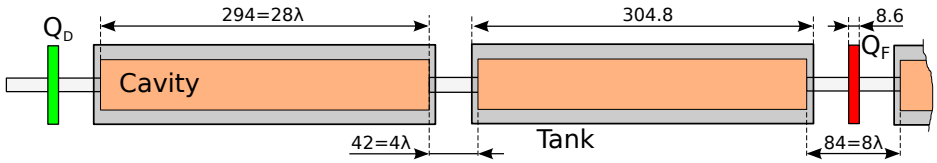

Figure 4.1. *Half of the periodic cell implemented in the simulation of the Linac, the following half is symmetric. All the values are expressed in* cm. *Two cavities are placed in between the focusing and defocusing quadrupoles.*

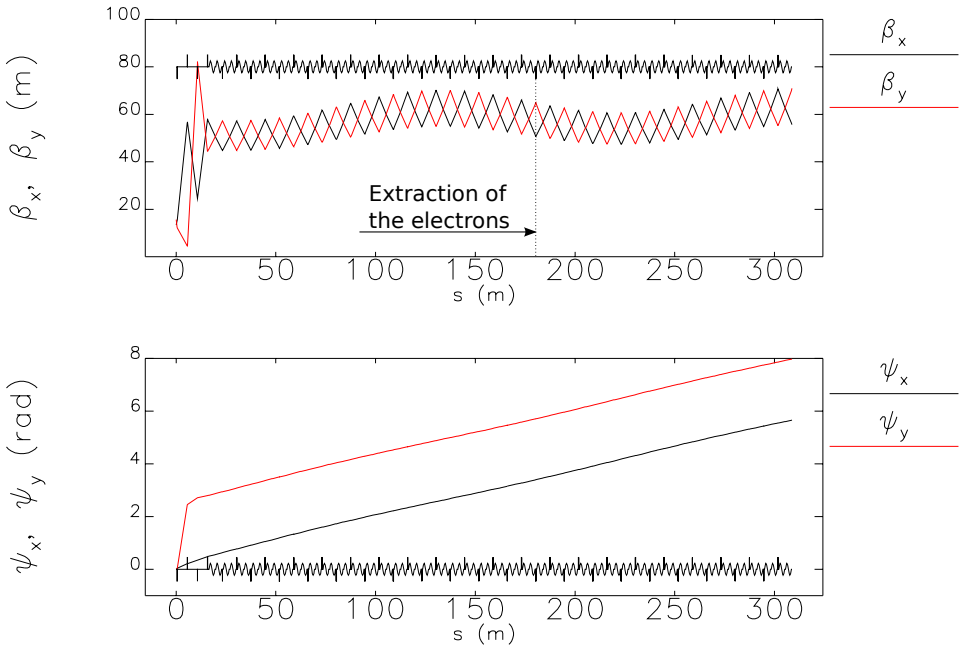

Figure 4.2. *β functions and phase advance along the Linac.*

All the Linac quadrupoles have the same normalized gradient [1] , so the optical functions keep their mean values along the full Linac and the

1 $k = \frac{eg}{p} = \frac{g}{B\rho}$ where e is the particle charge, g is the field gradient, p is the particle momentum and Bρ is the magnetic rigidity. A quick way to convert k to g is to use the formula:
$g = 3.3356\ k\ p; \qquad p[GeV/c].$

phase advance grows constantly. Note that the Linac focusing is quite weak, the maximum gradient of 9 T/m is required by the magnet at the end of the Linac where the energy of the beam is 6.7 GeV.

4.3 ORBIT CORRECTION

Real machines are never perfectly aligned. Elements are always shifted and tilted with respect to the reference orbit and parasitic fields fast drive the bunch far from the reference trajectory. This leads the emittance to increase and distorts the phase space, especially in presence of wake fields. On a long line it is extremely important to provide monitoring and correction of the orbit. This is done respectively using Beam Position Monitors (BPMs) and dipole correctors.

4.3.1 Intensity and Effects of Misalignments

Alignment errors in the position of the focusing magnets and of the cavities have been introduced along the Linac. The cavities have been shifted in both vertical and horizontal directions by random values taken from a Gaussian distribution with cuts at 3σ and $\sigma = 500$ μm, the same for the quadrupoles but their distribution has $\sigma = 100$ μm. No tilts were introduced at this time as *elegant* does not provide support for tilting elements in a native way as for the misalignments, moreover their effect is expected to be small.

The simulation has been run on the full Linac up to 6.7 GeV using the positron bunch coming out from the chicane. The Linac RF phase is 89° (the peak is at 90°, refer to Sec. 5.3) and wake fields were turned on.

Fig. 4.3 presents 200 orbits computed for different sets of alignment errors before correction. Fig. 4.4 reports the distribution of the RMS values of the position of the orbit at the BPMs (one each four cavities), made up from 1500 errors sets.

4.3.2 Correction Schemes

A first attempt to correct the orbit was made introducing a BPM and a corrector alternated in the spaces between the cavities free from the

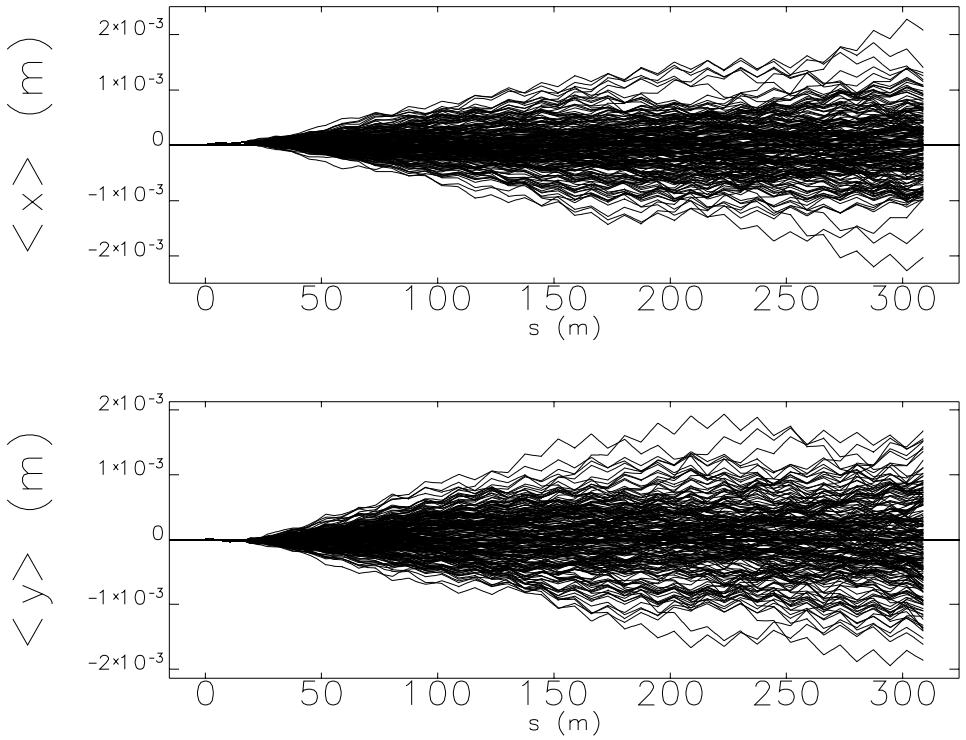

Figure 4.3. *Centroids of the bunch along the Linac in presence of misaligments and without correction. The ensemble is made up of* 200 *sets of random misaligments.*

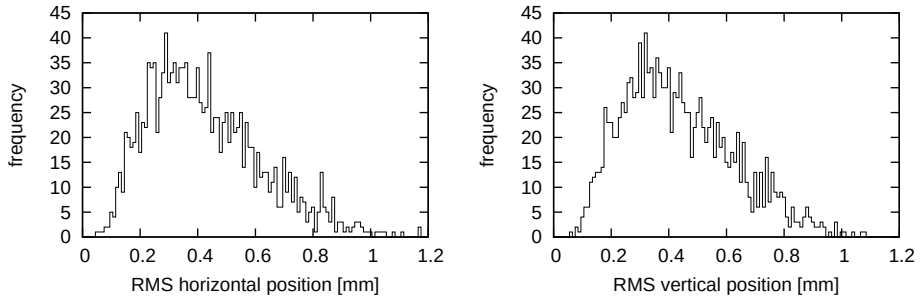

Figure 4.4. *Histogram of the RMS of the beam centroid positions at the monitors (one each four cavities) for* 1500 *ensambles of misalignments. The orbits are before correction.*

quadrupoles. BPMs and correctors were placed each four cavities and they were spaced by two cavities from each other. This is sketched in Fig. 4.5, this scheme was called *2:2 scheme* because of the regular spacing of two cavities between a BPM, a corrector and the next BPM. As the Linac contains 82 cavities, the total number of monitors is 21 and the same for correctors.

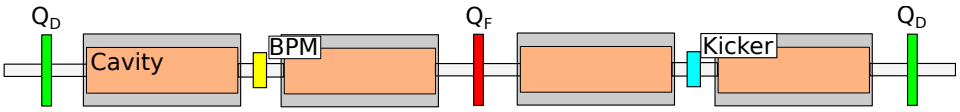

Figure 4.5. *Scheme of the 2:2 placement of the BPMs and kickers in the fodo cell of the Linac.*

As shown in Fig. 4.6 this scheme has a poor efficiency. Due to the regular spacing between monitors and correctors, the orbits are centred at the monitors but have a peak of the oscillation between them. The maximum orbit displacement is similar to the one before correction.

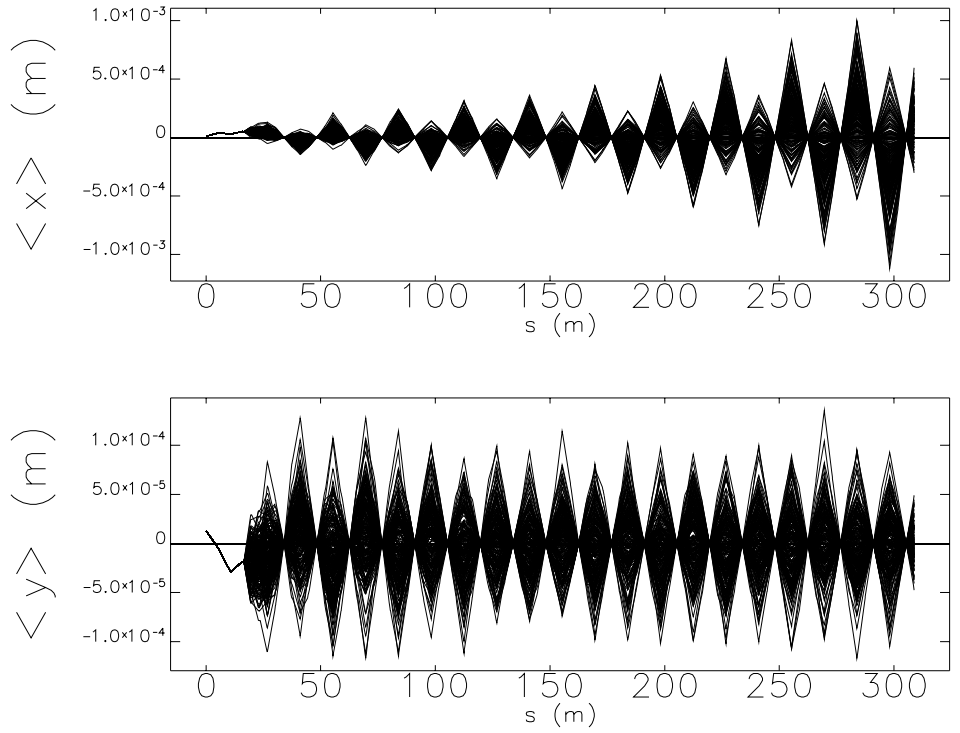

Figure 4.6. *Centroids of the bunch along the Linac in presence of misaligments and corrected with the 2:2 scheme. The ensemble is made up of* 200 *sets of random misaligments.*

To improve the correction scheme BPMs and correctors have been set up in the *1:3 scheme*. In this scheme BPMs and correctors are placed each four cavities as before, but the distance between the corrector and the BPM is alternatively one cavity and three cavities, as shown in Fig. 4.7.

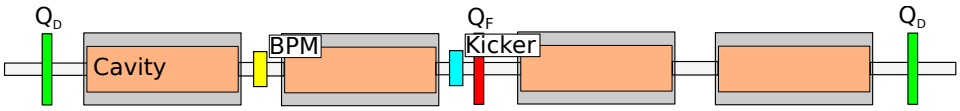

Figure 4.7. *Scheme of the 1:3 placement of the BPMs and kickers in the fodo cell of the Linac.*

The corrected orbits shown in Fig. 4.8 are now much smaller and their oscillations are comparable to the statistical movements of the centroid in the perfectly aligned case. Fig. 4.9 reports the distribution of the RMS values of the position of the orbit at the BPMs, made up from 1500 errors sets and corrected with the 1:3 scheme.

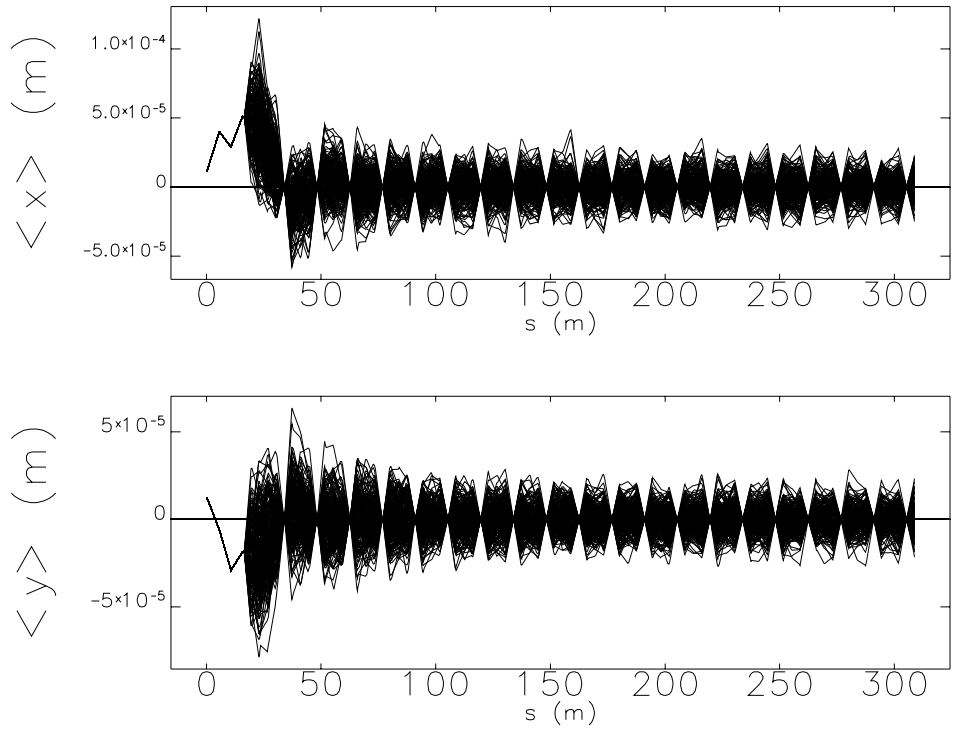

Figure 4.8. *Centroids of the bunch along the Linac in presence of misaligments and corrected with the 1:3 scheme. The ensemble is made up of 200 sets of random misaligments.*

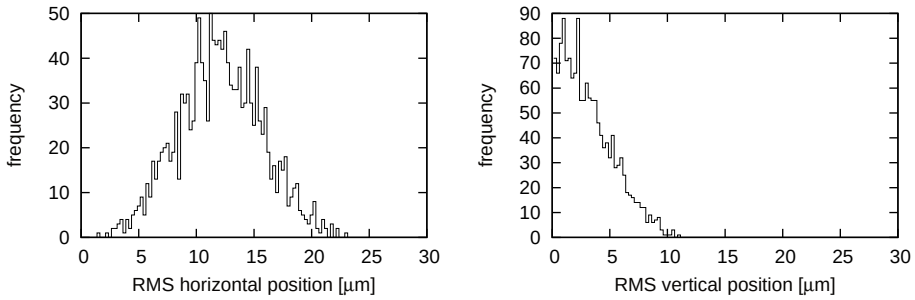

Figure 4.9. *Histogram of the RMS of the beam centroid positions at the monitors for* 1500 *ensebles of misalignments. The orbits are corrected with the 1:3 scheme.*

4.3.3 Results

Tab. 4.1 summarizes the results described above. The fully aligned Linac is compared to the one with alignment errors before and after corrections. The emittances are not shown in the table since they are not affected by the alignment errors. The 1:3 correction scheme is very efficient, in fact it reduces the peak value of the orbit and its RMS value at the monitors by a factor ~ 10. The 2:2 correction scheme is not effective since it limits the RMS value of the orbit at the monitors but it cannot contain the peak orbit value. Moreover the 1:3 scheme has RMS corrector strengths lower by a factor ~ 10 with respect to the 2:2.

	Aligned	Before corr	Corr 2:2	Corr 1:3
x peak [m]	$6.1 \cdot 10^{-5}$	$1.2 \cdot 10^{-3}$	$5.9 \cdot 10^{-4}$	$8.2 \cdot 10^{-5}$
y peak [m]	$9.5 \cdot 10^{-6}$	$1.3 \cdot 10^{-3}$	$8.9 \cdot 10^{-5}$	$3.4 \cdot 10^{-5}$
RMS x moni [m]	$1.2 \cdot 10^{-5}$	$7.0 \cdot 10^{-4}$	$1.7 \cdot 10^{-5}$	$1.7 \cdot 10^{-5}$
RMS y moni [m]	$1.0 \cdot 10^{-6}$	$7.1 \cdot 10^{-4}$	$6.2 \cdot 10^{-6}$	$6.2 \cdot 10^{-6}$
RMS x kick [rad]	-	-	$8.7 \cdot 10^{-5}$	$4.4 \cdot 10^{-6}$
RMS y kick [rad]	-	-	$1.0 \cdot 10^{-5}$	$3.0 \cdot 10^{-6}$

Table 4.1. *Summary table of the orbit correction in the Linac. The RMS values of the position at monitors and angle of the correctors are computed for each of the* 1500 *error ensambles as well as the maximum orbit displacement (peak). The data in the table are the threshold values below wich the* 90% *of the distributions are contained. The position of the centroid in the aligned Linac has a small oscillation due to the bunch distribution.*

For the scheme 1:3 the orbit after correction is very small with respect to the aperture of the vacuum chamber, the strengths of the correctors are a fraction of the foreseen ones ($8 \cdot 10^{-5}$ rad at the maximum energy) and the emittances are preserved. The tilts of the elements have not been considered since we expect a similar effect, or lower, on the orbit and on the emittances. We can conclude that for these values of the alignment errors the orbit correction is very good.

5 OPTIMIZATION

Big efforts are being putting into the increase of the dynamical aperture of the main rings. However at the moment the acceptance of momentum deviation is $\pm 1\%$, so the momentum spread of the bunches must be minimized to provide an efficient injection. Containing the longitudinal and transverse extensions of the bunches is critical not only to be able to inject, but also to reduce the oscillations to be damped in the main rings; indeed, injecting new particles during collision, this kind of oscillations would lead to a reduction of the luminosity. This is done tuning the parameters of the bunch compressor in order to reach the best compromise between the bunch length and momentum spread at the entrance of the Linac and so the minimum momentum spread at the end of it. In this chapter we will discuss how this has been done, providing also estimation of the momentum spread variations due to deviations from optimal values of the parameters.

5.1 DETERMINATION OF THE WORKING POINT

As the acceleration is lower for the electron beam, its final momentum spread will be higher than the one of the positron beam. So the optimization of the electron beam is overriding.

The geometrical parameters of the bunch compressor, discussed in Sec. 3.2, are summarized by the R_{56} parameter (see Eq. 2.20) which gives the path length dependence on the particle energy. The R_{56} depends both on the angle and on the drift length L_1. For simplicity the R_{56} was varied changing the angle only, the distance L_1 was fixed to 3 m. This ends up in the minimization of the field in the dipoles while containing the total length. A separation of ~ 2 m at the centre of two branches of the chicane has been maintained to leave space for access between the central dipoles.

The parameters of the cavity of the bunch compressor are determinant in the final result. The operating frequency comes from the geometry of the cavity. The S-band has been chosen as this technology do not

need any further R&D and are these cavities are used also for the main Linac. The radio frequency (RF) phase has been fixed at 0° in order to use the linear part of the RF voltage and minimize the non linearity in the energy-position correlation which may reduces the compression efficiency. Definitely the only free parameter of the cavity is the voltage.

To determine the working point, a bunch has been tracked from the exit of the Damping Ring to the end of the Linac. The effect of the CSR has been taken into account. The optimization was done without wake fields because the provided Green's functions were only 10 mm long, so one has to compress the bunch in a way that all the particles are within this length in order to be able to compute their effect. The simulation has been run on a grid of different α angles and voltages for the cavity, searching for the minimum momentum spread at the end of the Linac for both electron and positron beams.

The values of $\Delta p/p$ are shown in Fig. 5.1 for both electrons and positrons. In the centre of the plot of the electrons there is an area of values of voltage and angle where the momentum spread is minimum. A very high voltage produces useless-extra momentum spread, while if the voltage is too low, compression is not effective even for high values of R_{56} thus resulting in extra momentum spread produced in the Linac.

The starred points A, B and C are reported in coincidence on both positron and electron plots as the beams share the same cavity and splitter and combiner magnets, so the same working point has to be chosen for both of them. Tab. 5.1 reports the details of the starred points which can be chosen as working point as they minimize the $\Delta p/p$ of the electron beam. Between these points the values of both bunches do not vary so much, but some trends can be identified, for example at the point A the electron bunch is a little longer but has less momentum spread than the bunch at point C, however the difference is just 2% and therefore the point C was chosen as working point. It has the lower value of the angle, i.e. of the magnetic field in the dipoles and it is also the most favourable for the positrons whose $\Delta p/p$ improves of 7% from A to C. At the working point C, the momentum spread of the positron beam is not at its minimum, but due to the higher acceleration is still much lower than the one of the electron beam. The values of the coordinates of the point C are: 18.5 MV. 19°.

Fig. 5.2 shows the x and y slices of Fig. 5.1 from point C for both positrons and electrons. They present a reference for the momentum spread stability with respect to voltage and angle changes. They have

been fitted with a second-order-polynomial function; the agreement is quite good.

Tab. 5.1 presents also a comparison between wake fields on and off. For the bunch charge that travels the injector of SuperB (300 pC) their effect is small, but noticeable especially on the momentum spread.

Electron Bunch		A	B	C
Coordinate	Voltage	16.5 MV	17.5 MV	18.5 MV
	α angle	20.0°	19.5°	19.0°
Wake Fields OFF	$\Delta p/p$	1.44 ‰	1.45 ‰	1.47 ‰
	Bunch Length	0.65 mm	0.62 mm	0.59 mm
	ε_x	5.52 nm	5.52 nm	5.52 nm
	ε_y	47.9 pm	47.9 pm	47.9 pm
Wake Fields ON	$\Delta p/p$	1.46 ‰	1.48 ‰	1.51 ‰
	Bunch Length	0.65 mm	0.62 mm	0.59 mm
	ε_x	5.52 nm	5.52 nm	5.52 nm
	ε_y	47.9 pm	47.9 pm	47.9 pm
Positron Bunch		**A**	**B**	**C**
Coordinate	Voltage	16.5 MV	17.5 MV	18.5 MV
	α angle	20.0°	19.5°	19.0°
Wake Fields OFF	$\Delta p/p$	1.26 ‰	1.20 ‰	1.17 ‰
	Bunch Length	0.67 mm	0.63 mm	0.60 mm
	ε_x	4.21 nm	4.21 nm	4.21 nm
	ε_y	754 pm	755 pm	755 pm
Wake Fields ON	$\Delta p/p$			1.18 ‰
	Bunch Length	too long	too long	0.60 mm
	ε_x			4.22 nm
	ε_y			756 pm

Table 5.1. *Comparison between working points A, B and C indicated in Fig. 5.1 for the electron and the positron bunch.*

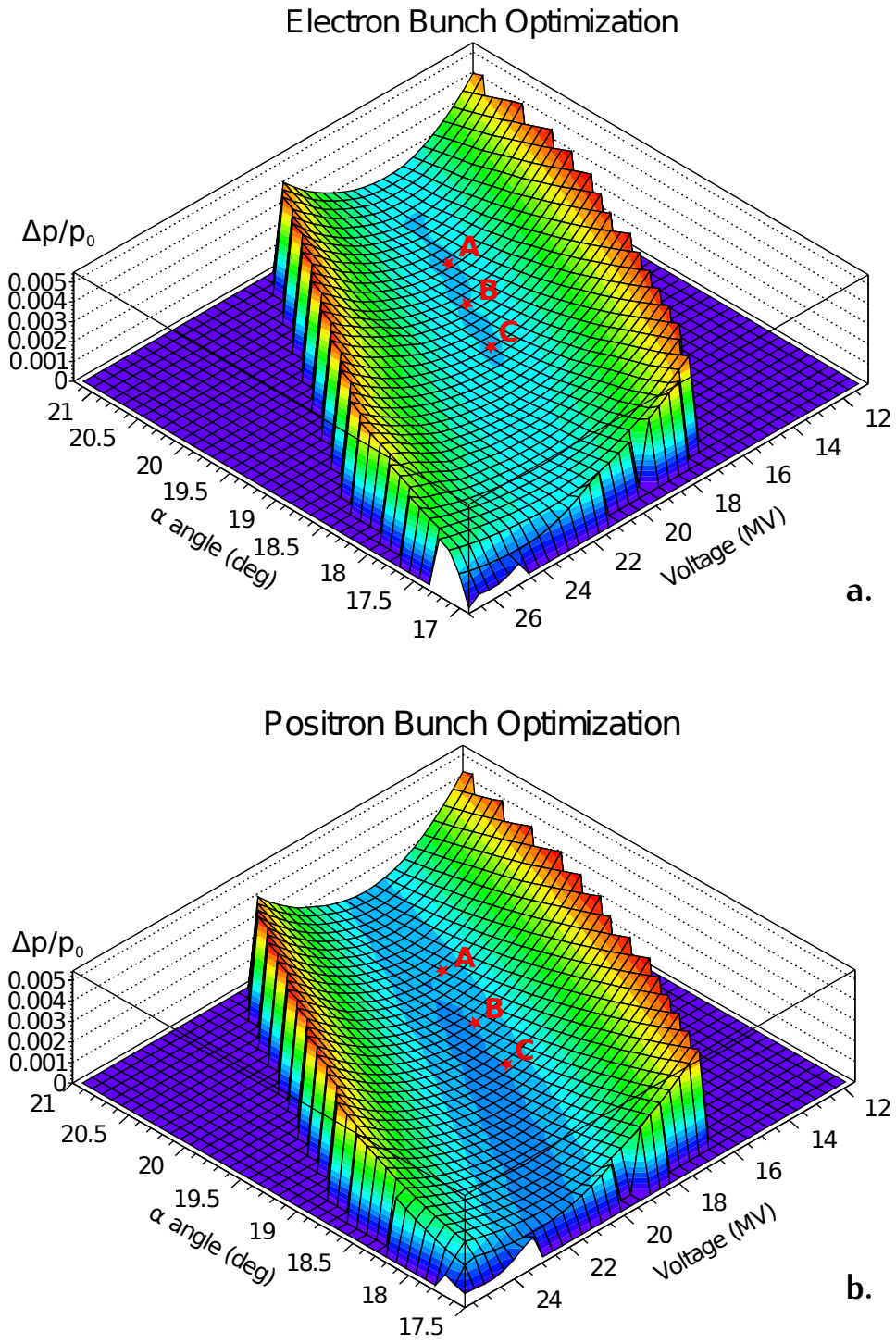

Figure 5.1. *Momentum spread of the electron bunch (a.) and of the positron bunch (b.) at the end of Linac plotted as function of the α angle of the chicane and of the voltage of the cavity. Starred points A, B and C indicate the same position in both plots. Refer to Tab. 5.1 for a detailed description of these points. Point C has been chosen as working point.*

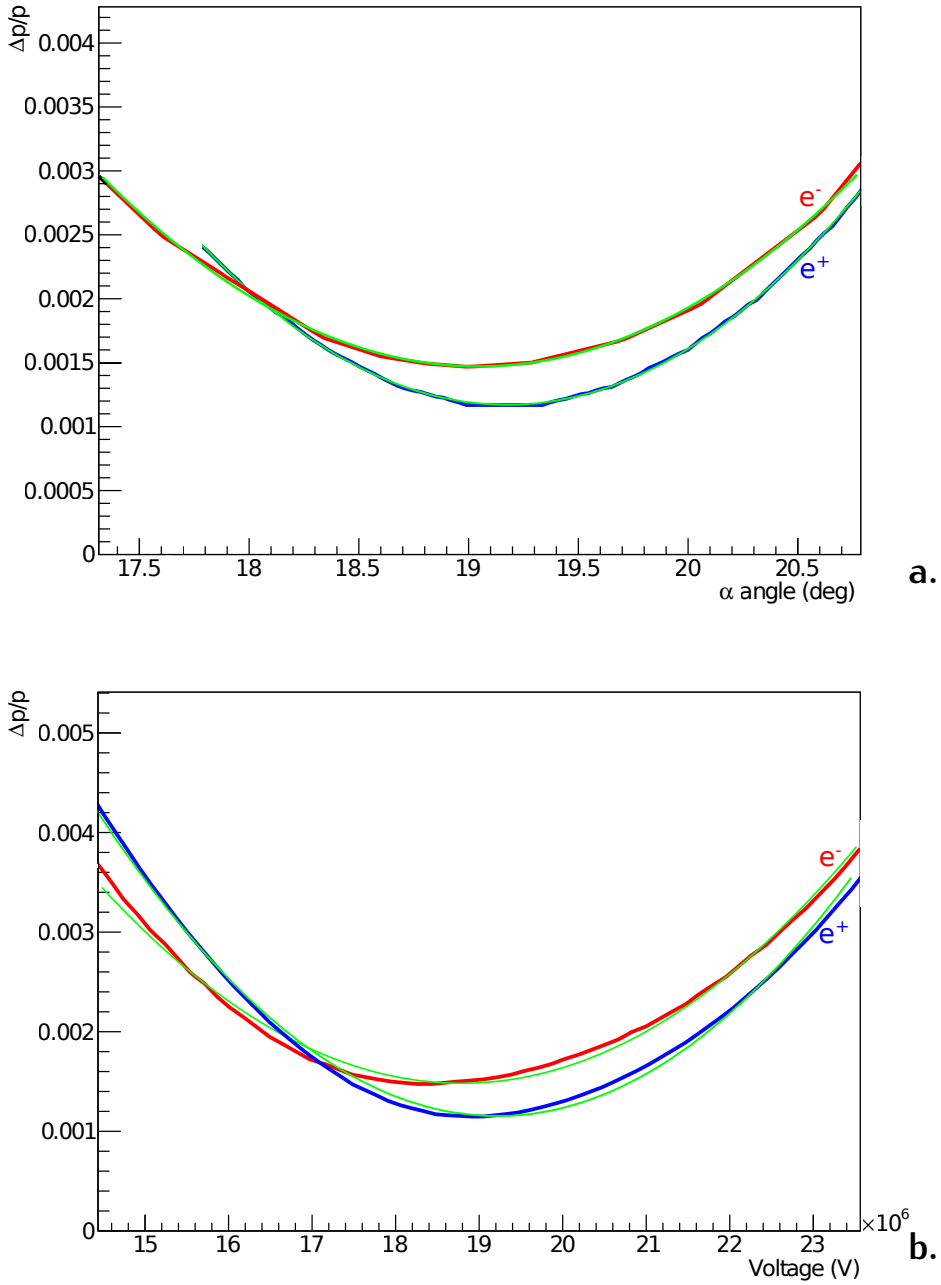

Figure 5.2. *Slices of Fig. 5.1 for both positrons and electrons from the point C. a:* $\Delta p/p$ *as function of the angle, the voltage is fixed at* 18.5 MV. *b:* $\Delta p/p$ *as function of the voltage, the angle is fixed at* 19.0 deg. *Blue and red lines are data of positrons and electrons respectively, green lines are second-order-polynomial fits.*

5.2 TEST WITH THE L-BAND CAVITY

The theoretical advantage of using an L-band cavity (at 1.428 GHz) for the compressor with respect to an S-band (2.856 GHz), is that fewer non linearities are introduced in the induced position-momentum correlation due to the longer period of 21 cm. A test of the compression that can be reached with these lower frequency cavities has been done. Again the objective is the reduction of the momentum spread at the end of the Linac especially for the electron beam. The geometry of the chicane was maintained as previously optimized, while the voltage of the cavity was varied to find the best values for this lower frequency.

As expected the smaller amount of non linearity, allows to reach a smaller momentum spread for both electron and positron bunches. The improvement is about 10%. However the minimum momentum spreads are obtained for quite different values of the voltage and as the cavity is shared by both the beams an average value has to be chosen. From Fig. 5.3 it's clear that this would destroy the benefits of an L-band cavity with respect to an S-band one, so the idea was discarded.

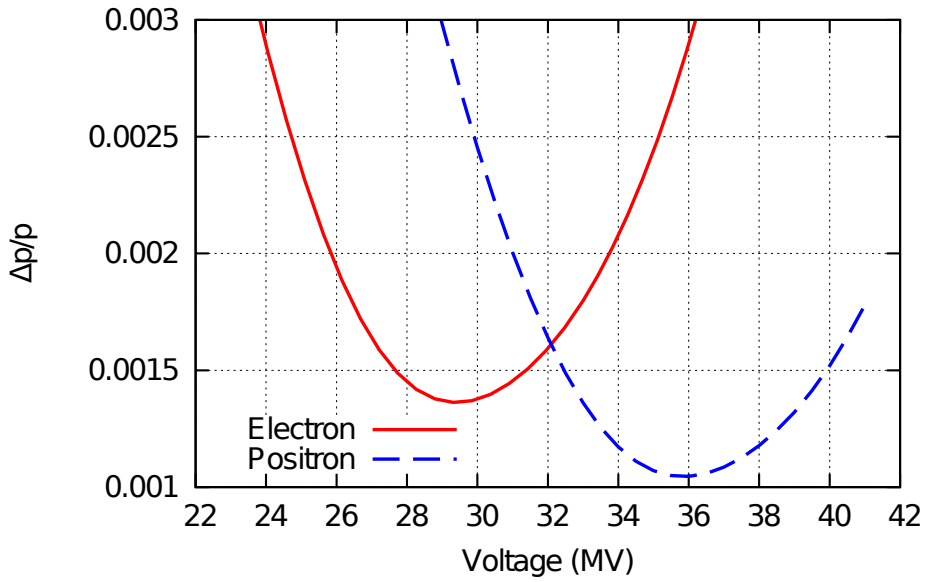

Figure 5.3. *Values of the momentum spread as function of the L-cavity voltage for electron and positron beams. The angle of the chicane is fixed at* 19°.

5.3 CHARACTERIZATION OF THE WORKING POINT

The longitudinal distributions of the electron beam for the working point C ($\alpha = 19°$, $V = 18.5$ MV) is shown in Fig. 5.4 at different positions along the injector. From a to b the bunch has travelled the transfer line from the damping ring which nearly preserve its shape. From b to c the bunch went through the zero-phased cavity which introduced the near linear (but actually sin-like) correlation between position and momentum. From c to d the bunch was longitudinally compressed due to the action of the chicane while the momentum spread is kept. Finally the adiabatic damping of the momentum took place in the Linac resulting in e.

Phase of the cavity of bunch compressor

In the ideal case bunches travel the RF cavity of the bunch compressor phased exactly at 0° (on the voltage zero crossing) to reduce non linearity in the induced position-momentum correlation and to obtain a more efficient compression. However, phasing the RF cavity of the bunch compressor to the centre of the bunch requires a stabilization system. To evaluate the requirements for this system, the tolerance with respect to small changes of the phase has been investigated.

Tracking both beams to the end of the Linac with different RF phases of the compressor, it was found that the momentum spread of both of them is quite stable with respect to changes of few degrees of the RF phase. Moreover, with the current layout of the transfer lines which slightly affects the phase space distribution, the momentum spread of the electron beam at the end of the Linac has a little improvement for a couple of degrees of positive phase (this means accelerating a little bit in the compressor). The positron beam has a nearly symmetric behaviour with respect to small phase changes. The final momentum spread dependence on the phase of the RF cavity is presented in Fig. 5.5.

At the minimum of the momentum spread, $\pm 1°$ shift of the phase of the cavity of the compressor causes a variation of $\pm 1‰$ in the momentum spread of the electrons and of $\pm 2‰$ in the one of positrons. It is clear that a stabilization to $\pm 1°$, easy to obtain with conventional systems, has a negligible effect on the momentum spread.

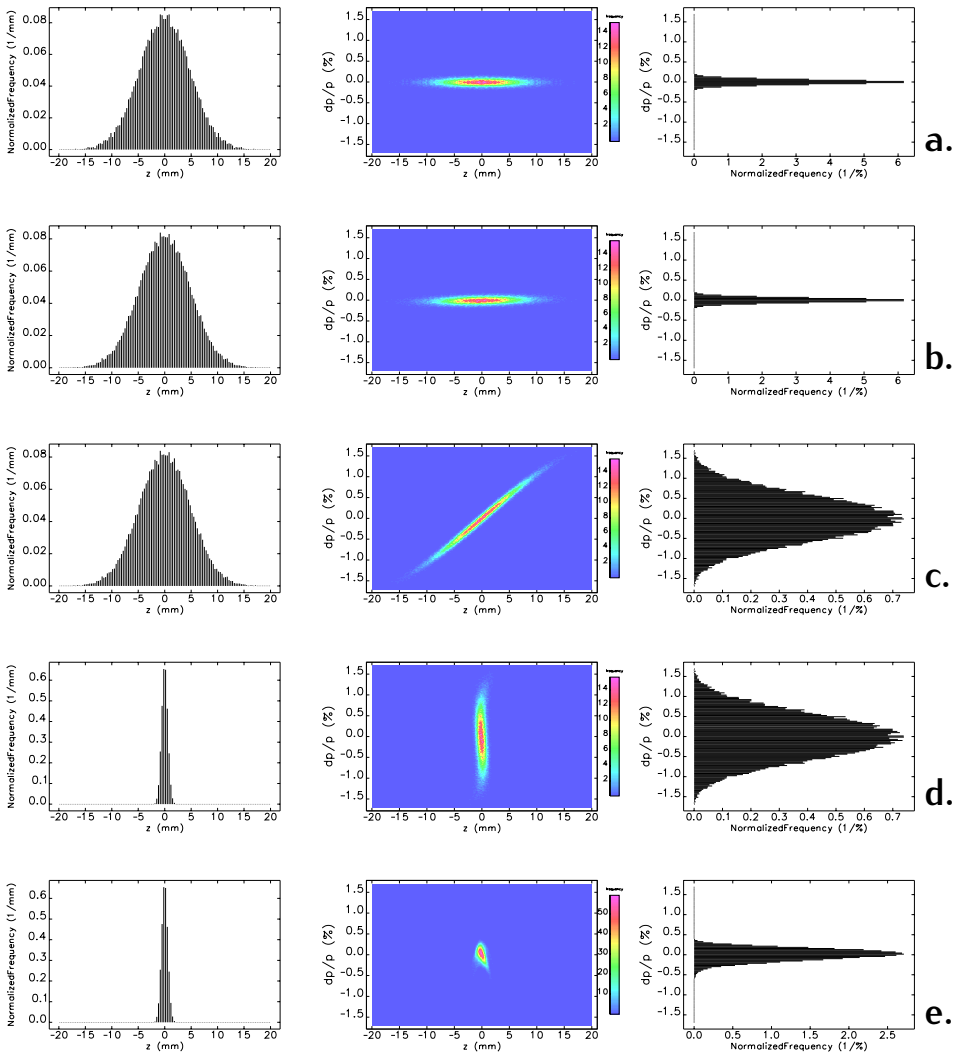

Figure 5.4. *Longitudinal-phase-space distribution of the electron bunch tracked at the working point. a: at the entry of the line. b: before the RF cavity. c: after the cavity. d: after the chicane. e: after the Linac.*
Note that all the plots have the same scales.

Phase of Linac

To obtain the maximum energy, the average of the positions of the particles in the bunch is placed on crest of the Linac RF voltage, the corresponding phase in the formalism of *elegant* is 90°. In this way the longitudinal phase space of the electron bunch at the exit of the Linac assumes the shape shown in Fig. 5.6.a which is a zoom of Fig. 5.4.e. It

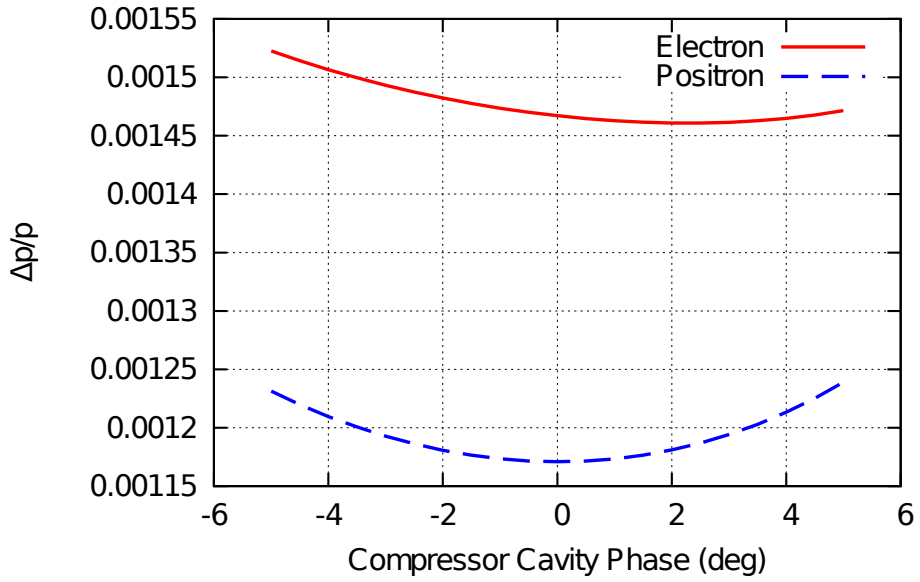

Figure 5.5. *Momentum spread at the end of the Linac for both positron and electron beams as function of the phase of the RF cavity of the bunch compressor. Positive phases imply acceleration, negative phases deceleration. The other parameters of the compressor are set at the working point.*

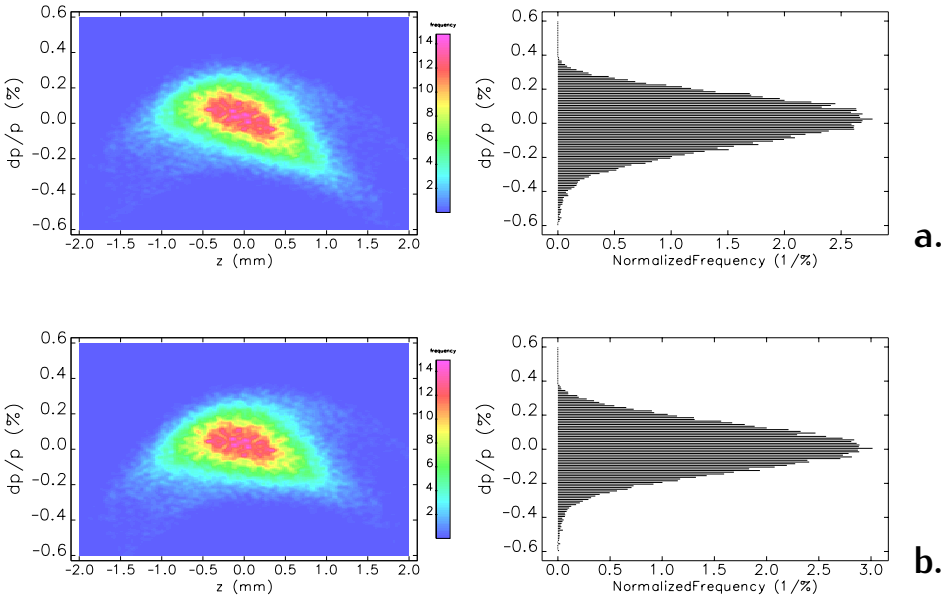

Figure 5.6. *Comparison of the longitudinal phase space of the electron bunch after the acceleration through the Linac phased at 90° (a.) and at 89° (b.).*

is possible to notice that the tail of the bunch (positive z) has a lower energy which increases the total momentum spread. This is due to the shape that the bunch has after the compressor.

The low energy tail may be avoided by changing the phase of the Linac RF cavities, leading to a reduction of the momentum spread. This has been investigated and results are presented in Fig. 5.7. The momentum spread of both beams is reduced by advancing the phase from 90° (on crest acceleration) to 89° while their final energies are practically unchanged. Fig. 5.6.b shows the electron beam tracked along the Linac phased at 89°.

At the minimum of the momentum spread, ±1° shift of the phase of Linac causes a variation of ±3.3% in the momentum spread of the electrons and of ±6.2% in the one of positrons. To keep the momentum spread near its minimum a stabilization system at 0.5° will be required. The final energy is stabilized acting on the voltage of the cavities however the effect of ±1° phase shift on it, is negligible.

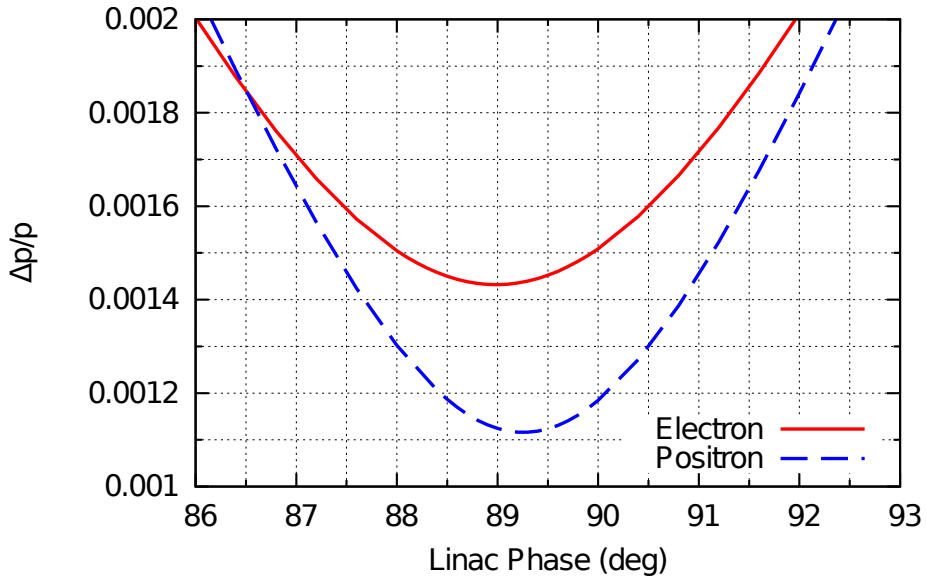

Figure 5.7. *Momentum spread as a function of the phase of the Linac RF voltage for both electron and positron beams.*

5.4 TEST WITH INCREASED BUNCH CHARGE

Increasing the charge per bunch of the positron beam is difficult and raises the costs of the production system. On the other hand, the bunch charge of the electron beam (which is directly produced by the gun) used for the SuperB injection system design, is quite low with respect to the injector capabilities and could be easily raised.

The effects of a higher bunch charge on the transport and acceleration of the beams extracted from the damping ring have been investigated. An higher charge intensifies the collective phenomena like CSR and wake fields, leading to a higher energy redistribution within the bunch. However, depending on how energy and charge are distributed within the bunch, this may also be positive.

The emittance and the momentum spread of the bunches at the end of the Linac have been estimated with *elegant* for different values of the bunch charge, for the working point selected in the Sec. 5.1. The final bunch length and the vertical emittance are nearly independent on the bunch charge with variations of few per thousand in the range 200 pC ÷ 1000 pC. On the other hand the momentum spread and the horizontal emittance have a small variation as shown in Fig. 5.8. The emittance increases with the bunch charge, while the momentum spread has a minimum for bunch charges of ~ 370 pC for the electrons and ~ 500 pC for the positrons. Reference values for 450 pC bunches are collected in Tab. 5.2.

	e^-	e^+
$\Delta p/p$	1.43 ‰	1.10 ‰
Bunch Length	0.59 mm	0.60 mm
ε_x	5.54 nm	4.24 nm
ε_y	48.0 pm	756.3 pm

Table 5.2. *Beam parameters at the end of the Linac computed with a bunch charge of* 450 pC.

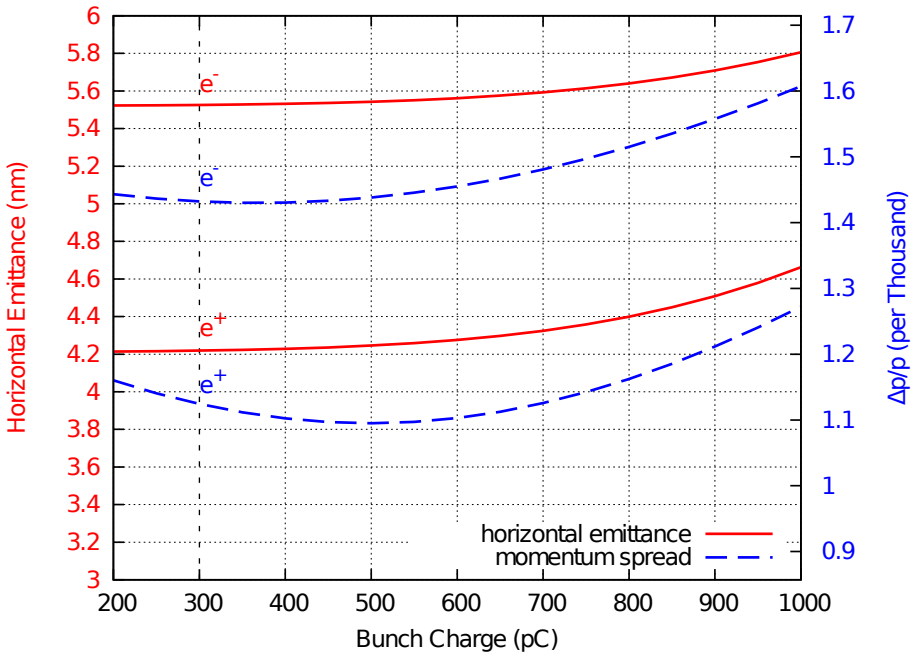

Figure 5.8. *Horizontal emittance and Momentum spread as a function of the bunch charge for both electron and positron beams. Bunch length and vertical emittance are nearly constant in this charge range.*

5.5 OPTIMIZED FINAL PARAMETERS

Tab. 5.3 and Tab. 5.4 collect all the parameters of the bunch compressor and of the Linac after the optimization.

Fig. 5.9 and Fig. 5.10 show the envelopes of the beams computed by tracking from the damping ring. The positron beam goes across 82 cavities to the end of the Linac at 6.70 GeV. The electron beam is tracked through 46 Linac cavities up to 4.18 GeV, then it travels a section of four matching quadrupoles and is injected in the second half of the injection cell of the Low Energy Ring, see Chap. 6 for a description of it.

The only place where the horizontal envelope rises up is the centre of the chicane due to the high dispersion which is necessary for the compression. The small envelopes along the whole injector are well inside the aperture of the elements ensuring few losses and contributing to the high efficiency of the injection.

Parameter	Symbol	Unit	Value
Operating energy	E	GeV	1.0
Cavity voltage	V	MV	19.5
Cavity frequency	f	MHz	2856
Cavity phase	ϕ	Deg	0
Magnets length	L_d	m	1.35
Magnets field	B	T	0.82
Curvature radius	R	m	4.07
Chicane arm length	L_1	m	3.0
Chicane central length	L_2	m	0.50
Chicane angle	α	Deg	19
chicane 1^{st} order matrix element	R_{56}	m	-0.918
chicane 2^{nd} order matrix element	T_{566}	m	1.580
Initial Bunch length (RMS)	$\sigma_{s\,i}$	mm	4.8
Final Bunch length (RMS)	$\sigma_{s\,f}$	mm	0.6
Initial Momentum spread (RMS)	$\Delta p/p_i$	‰	0.62
Final Momentum spread (RMS)	$\Delta p/p_f$	‰	5.18

Table 5.3. *Parameters of the bunch compressor after the optimization.*

Parameter	Symbol	Unit	e^-	e^+
Entering energy	E_i	GeV	1.00	
Exiting energy	E_f	GeV	4.18	6.70
Cavity gradient	V_m	MV/m	23.54	
Cavity frequency	f	MHz	2856	
Cavity phase	ϕ	Deg	89	
Number of cavities	N_c		46	82
Number of quadrupoles	N_q		26	44
Number of monitors	N_m		12	21
Number of correctors	N_k		12	21
Linac length	L_a	m	307	
Matching length	L_m	m	~ 15	
Total length	L	m	~ 322	
Maximum horizontal beta	$\beta_{x\,Max}$	m	~ 70	
Maximum vertical beta	$\beta_{y\,Max}$	m	~ 70	
Final hor. emittance	ε_x	nm	5.53	4.22
Final ver. emittance	ε_y	pm	47.9	756
Init. mom. spr. (RMS)	$\Delta p/p_i$	‰	5.18	
Final mom. spr. (RMS)	$\Delta p/p_f$	‰	1.43	1.12

Table 5.4. *Parameters of the Linac after the optimization.*

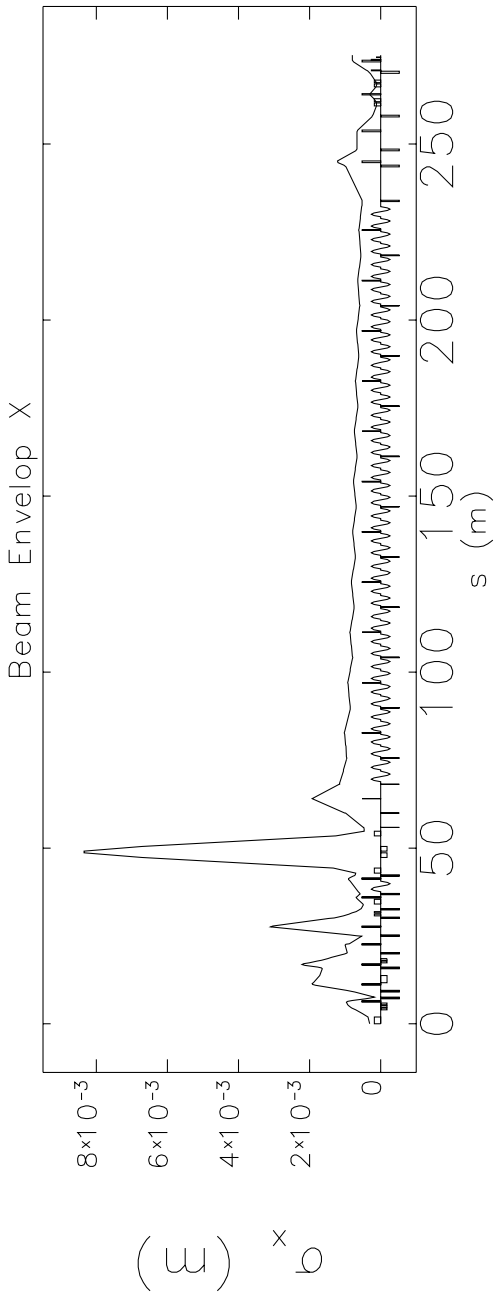

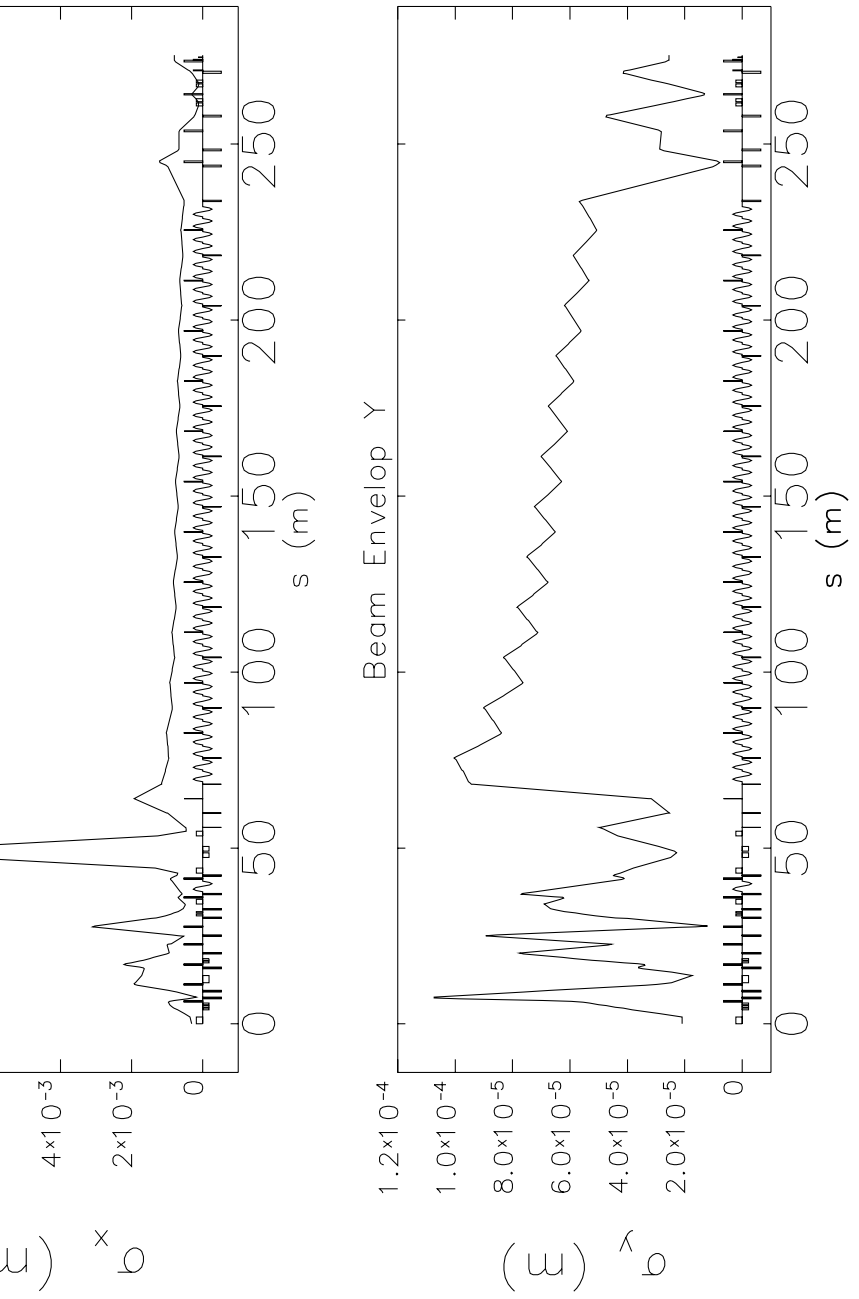

Figure 5.9. *Horizontal (top) and vertical (bottom) standard deviations of the distribution of the electron bunch from the exit of the damping ring to end of the injection cell of the Low Energy Ring. Please refer to Chap. 6 for a description of the injection cell.*

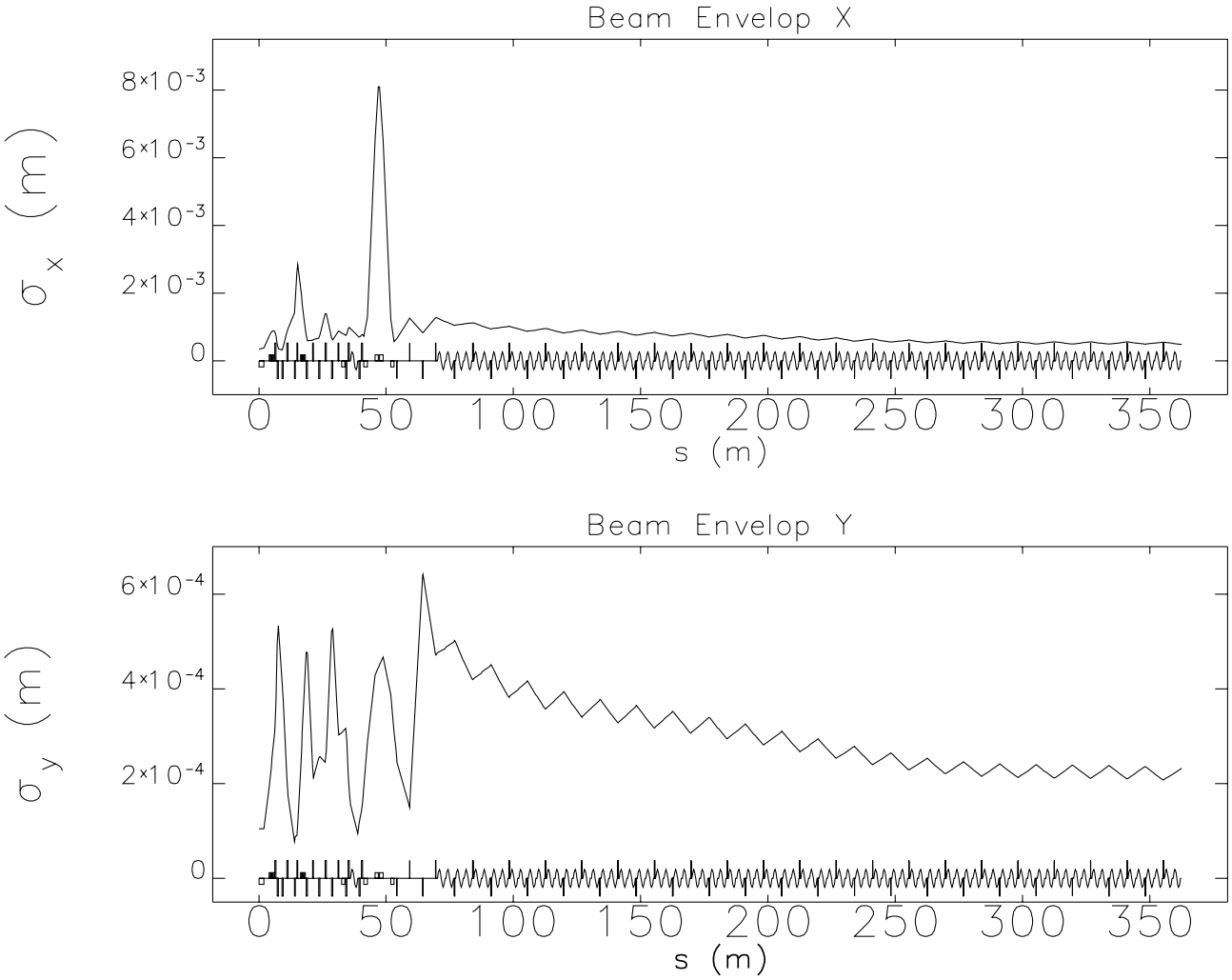

Figure 5.10. *Horizontal (top) and vertical (bottom) standard deviations of the distribution of the positron bunch from the exit of the damping ring to end of the Linac.*

6 INJECTION IN THE LOW ENERGY RING

The particles tracked along the full complex have to be injected in the main rings to compensate for the losses. This is a continuous process which aims to keep constant both beam currents and luminosity. In the following sections details about the injection of the electrons in the Low Energy Ring (LER) will be provided. The injection of positrons in the High Energy Ring (HER) is easier than that of the electrons due to the smaller horizontal emittance of the beam at the end of the Linac. The injection takes place in the horizontal plane and therefore the beam size and displacement in the horizontal phase space are the critical parameters.

6.1 THE INJECTION CELL

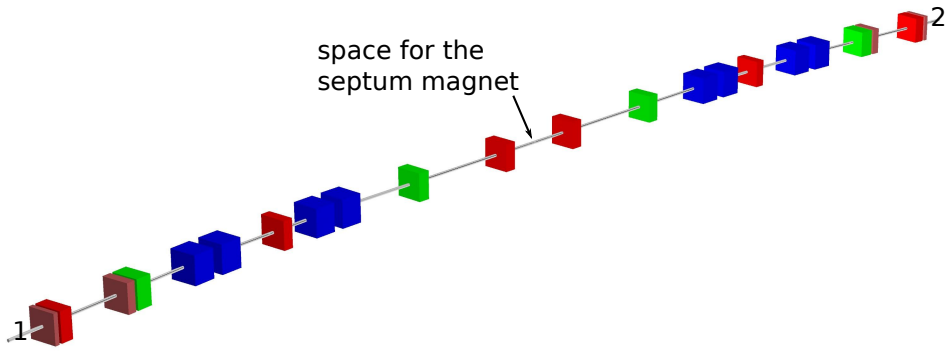

Figure 6.1. *View of the injection cell of the Low Energy Ring. Dipoles are blue, green and red objects are quadrupoles. Also four sextupoles are present, they are brown. Positions 1 and 2 host the kickers. The septum will be placed in the centre of the cell.*

The tracking was done using the latest lattice (*v*.16) of the LER. The section in which the injection takes place is presented in Fig. 6.1. It is symmetric with respect to the centre, where a septum dipole is placed.

This magnet will align the injected particles parallel to the reference orbit without affecting the stored beam, shielded by the septum. The septum of the magnet is placed at a distance equal to the horizontal acceptance of the ring that is 30 times the size of stored beam.

6.1.1 Principle of working

Two fast kickers are placed at the beginning and the at end of the cell (positions 1 and 2 in Fig. 6.1). The first kicker will give an angle to the stored beam displacing its orbit in the horizontal direction. After a phase rotation of: $(2n+1)\,\pi/2$, ($n = 1$ in this case) the bunch will travel parallel to the reference orbit with the maximum offset. This is used to bring the stored beam close to the septum, where the bunch coming from the Linac is injected. The stored and the injected bunches travel through the second half of the cell. At the end of it the second kicker restores the initial condition for the stored beam while the injected bunch is still a bit tilted and starts to oscillate around the reference orbit. The maximum amplitude of this oscillation is well within the ring acceptance and will be damped by the synchrotron radiation without losses of particles. Fig. 6.2 schematizes the acceptance shift at the septum provided by the kickers, the available phase space to inject the beam is highlighted by the blue ellipse.

Fig. 6.3 and Fig. 6.4 show the values of β and μ along the cell for the stored beam. Note that the total phase advance is 3π, while at the centre of the cell its value is $3\pi/2$.

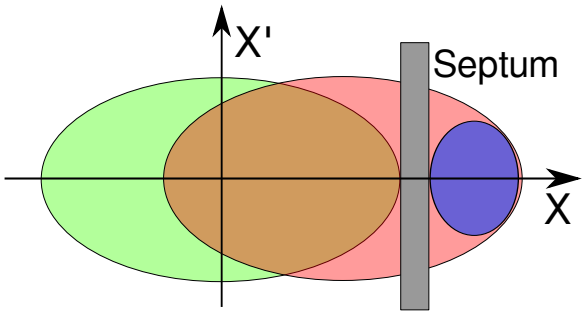

Figure 6.2. *Scheme of the acceptance of the machine at the septum in the x-x′ plane. The green ellipse represents the normal acceptance related to the stored orbit, the red one refers to the orbit shifted by the kickers and the blue one is the shape that the injected beam should have.*

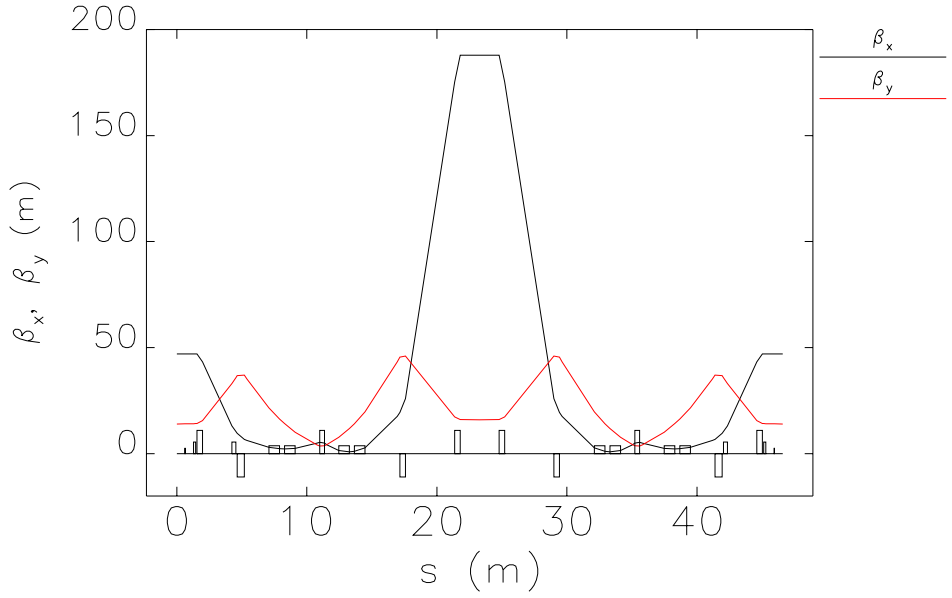

Figure 6.3. *Beta functions of the injection cell.*

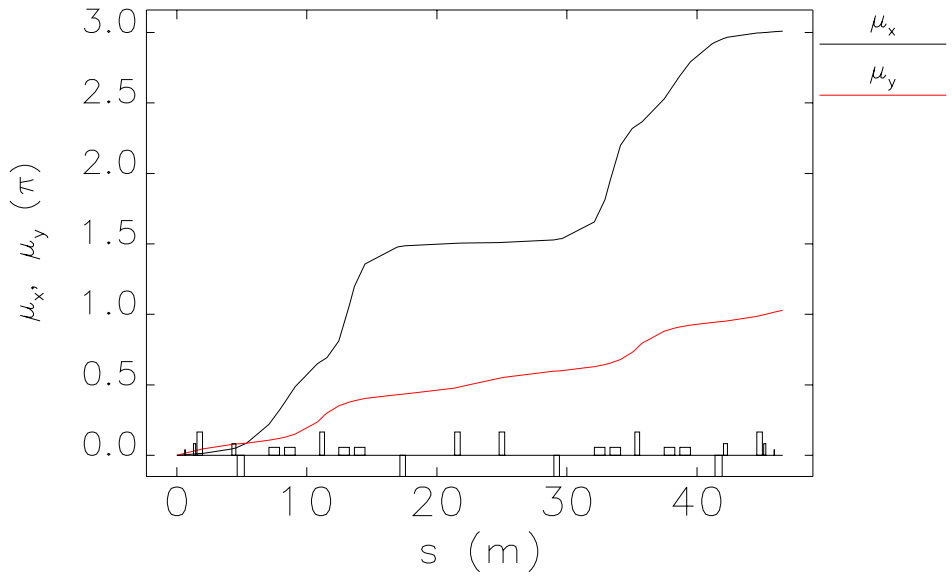

Figure 6.4. *Phase advances in the injection cell.*

6.1.2 Advantages from the Dispersion

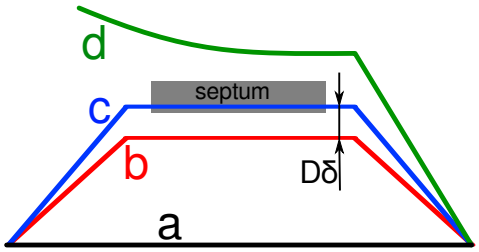

Figure 6.5. *a: normal orbit of the stored beam. b: kicked orbit of the stored beam. c: kicked orbit of the stored beam referred to energy of the injected beam (shifted due to the dispersion). d: injected beam trajectory.*

Small advantages in the injection can be taken also from dispersion in the injection cell. The idea is to have the dispersion function of the stored beam at a value different from zero at the septum in a way that if the energy of the stored bunch is, for instance, increased, it will pass closer to the septum. Now, if the energy of the injected bunch is tuned a bit higher than the nominal, its separation from the stored bunch will refer to the dispersion trajectory and so it will be smaller by $D\delta$, here $\delta = (p_{inj} - p_{sto})/p_{sto}$, refer to Fig. 6.5. This shift is then cancelled at the interaction point as the dispersion is zero there.

6.2 DETERMINATION OF THE INJECTION PARAMETERS

First of all the intensities of the two kicks have to be determined. The kicks must shift the stored beam from 30 σ_x^{sto} to 4 σ_x^{sto} distance from the septum and then center it again on the reference orbit. As the cell is symmetric, the kicks are equal.

Kicks can be estimated with the following equation:

$$\theta = \frac{x_{sept}}{\sqrt{\beta_i \beta_{sept}}}$$

which can easily be derived from the transport matrix equation 2.12 setting all the initial coordinates to 0 except $x_i' = \theta$. A check of the analytic computation was done with *elegant* to take into account the dispersion and the actual beam distribution.

The beam coming from the Linac has then to be matched. As shown by Eq. 2.13 and 2.14, it is convenient to match the α function to zero, while β should have an intermediate value in order to fit both σ_x^{inj} and

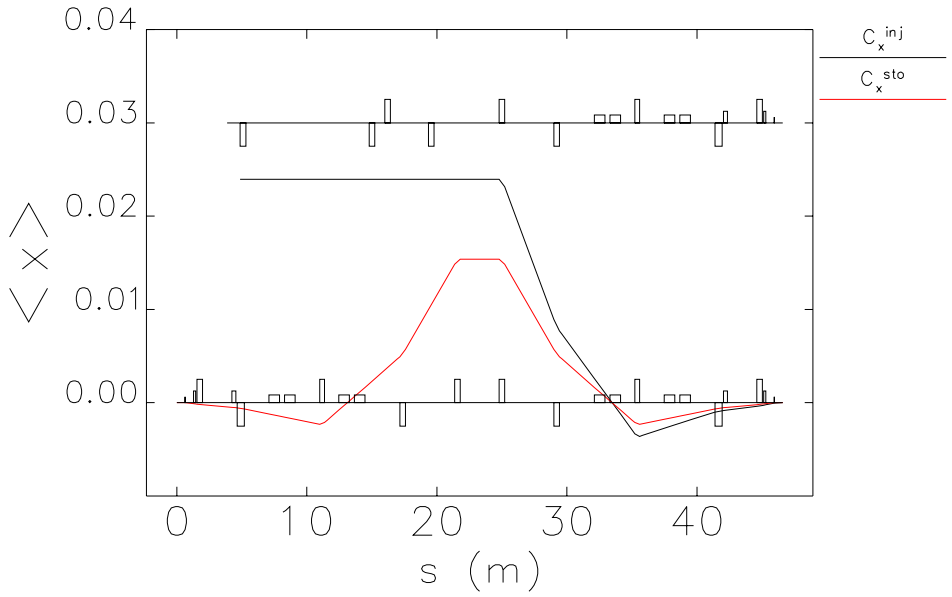

Figure 6.6. *Centroid displacement of both the stored (red) and the injected (black) bunches in the LER injection cell.*

$\sigma_{x'}^{inj}$ into the acceptance of the ring. A good value of the β function has been estimated at 80 m. Obviously the vertical optical functions are matched to the ones of the injection cell. The match will be done along the transfer lines from the Linac to the main rings, but for the moment four quadrupoles in a straight path have been used.

Finally the correct offset must be provided for the injected bunches with respect to the reference orbit of the rings. This must ensure a $3\sigma_x^{inj}$ separation between the centroid of the bunches and the septum wall.

The optimization of the injection energy related to the dispersion of the injection cell will be done in future according to the definitive value of the dynamical aperture of the rings. The parameters used are summarized in Tab. 6.1.

Fig. 6.6 shows the displacement of the centroids of both the stored and the injected beam along the lines. Note that the stored beam crosses the centre of the pipe four times: each time the phase becomes $n\pi$. The injected beam goes through four quadrupoles matching the optical functions as explained before, then travels the second half of the injection cell with the given offset.

Parameter	Symbol	Unit	Value
Stored Beam Energy	E_{sto}	GeV	4.18
Injected Beam Energy	E_{inj}	GeV	4.18
Horizontal stored emittance	ε_x	nm	2.46
Vertical stored emittance	ε_y	pm	6.15
Stored momentum spread	δ	‰	0.668
α_x at septum	α_x	-	0
β_x at septum	β_x	m	188
α_y at septum	α_x	-	0
β_y at septum	β_y	m	16.3
Kick angle	α_{kick}	mrad	0.163
Stored bunch size at septum	σ_x^{sto}	mm	0.598
Stored orbit shift at septum	$26\sigma_x^{sto}$	mm	15.4
Acceptance of the ring	$30\sigma_x^{sto}$	mm	17.9
Septum-orbit separation	$30\sigma_x^{sto}$	mm	17.9
Septum thickness	ΔS	mm	4
Injection β_x	β_x^{inj}	m	80
Injected bunch size at septum	σ_x^{inj}	mm	0.668
Septum-centroid separation	$3\sigma_x^{inj}$	mm	2.00
Injection offset	C_x^{inj}	mm	23.9
Centroid-centroid separation	$C_x^{inj} - C_x^{sto}$	mm	8.4

Table 6.1. *Summary of the injection values and parameters of the Low Energy Ring, lattice v.16.*

6.3 PHASE SPACES OF THE INJECTION

Horizontal Phase Space

Fig. 6.7 presents the x phase space of the beams both at the septum and at the end of the injection cell. It's possible to note the $3\pi/2$ rotation of the injected beam. The acceptance of the machine is shown in Fig. 6.8 where it's clear that the injected bunch is widely stored in the ring.

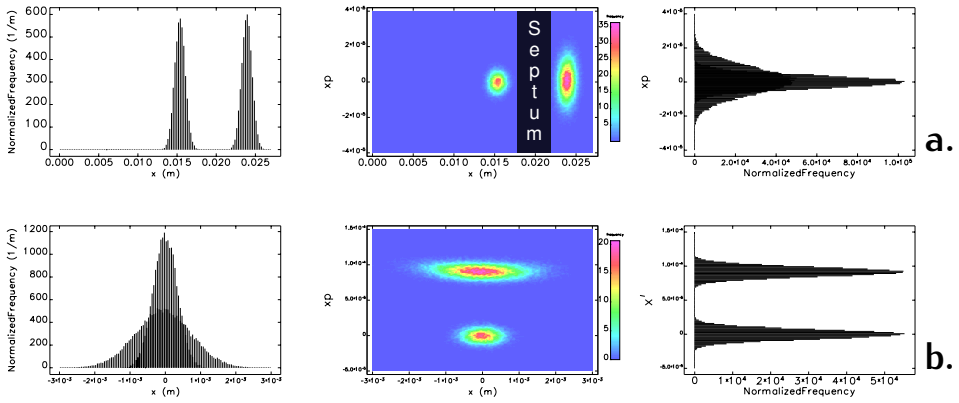

Figure 6.7. *Horizontal-phase-space distribution of the stored (smaller) and injected (bigger) beam. a: imediately after the septum. b: at the end of the injection cell.*

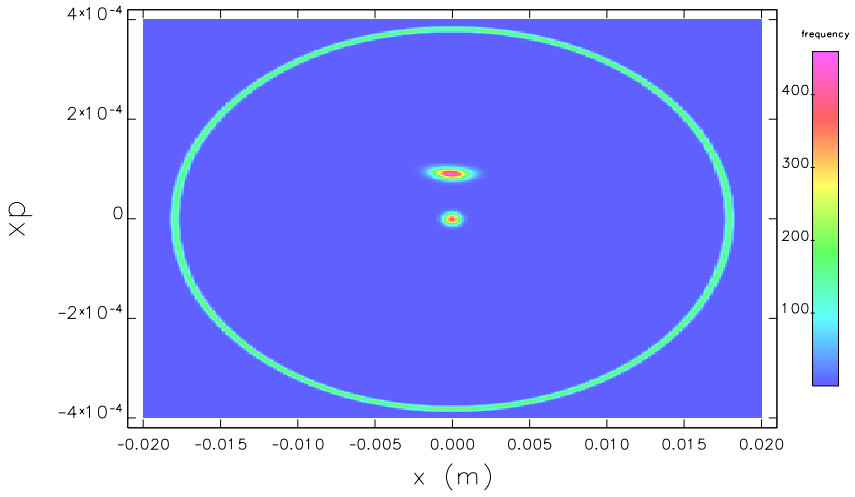

Figure 6.8. *x phase space of the stored and the injected beam at the end of the injection cell plotted within the ring acceptance.*

Vertical Phase Space

The vertical coordinate of the injected beam is aligned to the stored one, so it is easier to inject it. However a check also of the y phase space has been done. The result is shown in Fig. 6.9 where the vertical

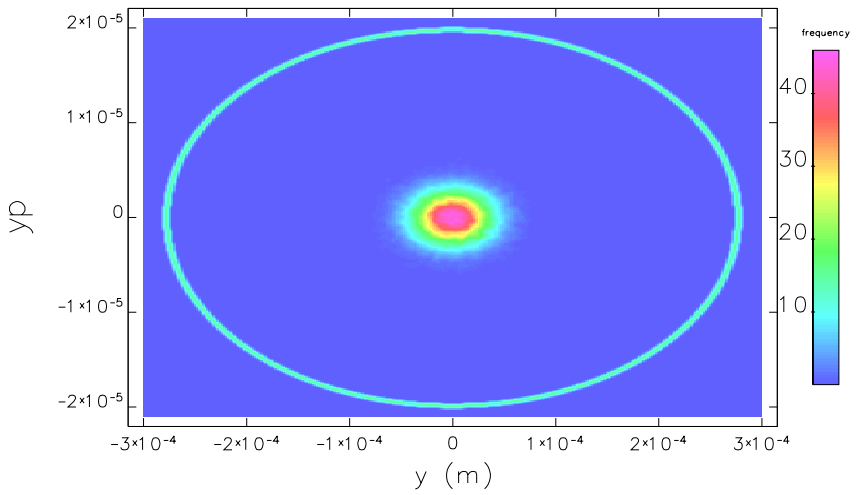

Figure 6.9. *y phase space of the injected beam at the end of the injection cell plotted within the ring acceptance.*

coordinates of the injected beam are compared with the acceptance of the ring assumed at 30 σ_y^{sto}. The beam is widely inside the acceptance.

Longitudinal Phase Space

The bunch length of the beams stored in the main rings is 5 mm, much longer than the acceptance of the Linac so there is no need to check. Concerning the momentum spread, the ring acceptance is $\delta_{max} \approx \pm 1\%$. This is $\approx 7\sigma_\delta$ of the injected electron beam whose distribution is nearly Gaussian and allows the injection of 99 % of the beam: $3\sigma_\delta^{inj}$ plus some margin for energy errors in the Linac. For a visualization of the longitudinal phase space, please refer to Fig. 5.6.b in Sec. 5.3.

7 CONCLUSIONS

A start-to-end tracking from the damping ring to the main rings has been done using *elegant*. Both electrons and positrons beams were studied. CSR and wake fields effects were taken into account respectively in the compressor and in the Linac.

The parameters of the compressor and the acceleration phase were optimized in order to achieve the minimum momentum spread at the end of the Linac. An effective correction scheme for the orbit in the Linac was provided. The injection of the electrons (the critical beam) in the Low Energy Ring was studied.

7.1 SUMMARY OF THE RESULTS

- The optimized bunch compressor is capable to allow the acceleration in the Linac with a resulting momentum spread acceptable for the injection in the main rings. Tab. 5.3 and Tab. 5.4 collect the parameters of the bunch compressor and of the Linac.
- The beam dynamics effects of CSR and wake fields have been verified to be negligible for the bunches that travels the injector of SuperB, due to their charge of 300 pC. Increasing the bunch charge to more than 600 pC will boost the collective effects reducing the efficiency of the injection, as studied in Sec. 5.4.
- An effective scheme for the orbit correction in the Linac was studied, it is presented in Sec. 4.3.
- After the track in the full injector, the electron bunch was stored in the Low Energy Ring. The position in the phase space of the injected bunch is well within the acceptance of the ring proving the very high efficiency of the injector.
- The small envelope of the beam along all the injector (see Fig. 5.9 and Fig. 5.10 in Chap. 5) guarantees very low losses and an efficiency higher than 99%.

7.2 OUTLOOK

The following studies still need to be done on the injector:

- Match the transfer lines from the damping ring to the Linac in order to allow them to share some magnets.
- Design the transfer lines from the Linac to the main rings.
- Verify the injection of the positrons in the HER.
- Track the injected particles along the whole rings and verify their damping taking into account also the interaction at the IP as the injection is made while colliding.

BIBLIOGRAPHY

[1] M.E.Biagini, P. Raimondi, and J. Seeman, editors. *SuperB Progress Report - Accelerator*. INFN - Laboratori Nazionali di Frascati, December 2010. URL: http://arxiv.org/abs/1009.6178v3.

[2] Antoine Chanché. *Optimization of the bunch compressor for the SuperB*. technical report. INFN - Laboratori Nazionali di Frascati, 2010.

[3] Antoine Chanché. *Design of the Transfer lines going to and from the SuperB damping ring*. Technical report. INFN - Laboratori Nazionali di Frascati, 2010.

[4] M. Borland. "elegant: A Flexible SDDS-Compliant Code for Accelerator Simulation". In: *Advanced Photon Source LS* 287 (2000).

[5] *BaBar Collaboration Homepage*. URL: http://www.slac.stanford.edu/BF/.

[6] *Belle Collaboration Homepage*. URL: http://belle.kek.jp/.

[7] *The Collider Detector at Fermilab*. URL: http://www-cdf.fnal.gov/.

[8] SuperB Collaboration. *SuperB: A High-Luminosity Asymmetric e+ e- Super Flavor Factory. Conceptual Design Report*. Technical report. INFN - Laboratori Nazionali di Frascati, 2007. URL: http://www.pi.infn.it/SuperB/?q=CDR.

[9] P. Raimondi. "Status on SuperB effort". In: *Proceedings of the 2nd SuperB Workshop*. Frascati, Rome, Italy, 2006. URL: http://www.lnf.infn.it/conference/superb06/talks/raimondi1.ppt.

[10] P. Raimondi, D. Shatilov, and M. Zobov. *Beam-Beam Issues for Colliding Schemes with Large Piwinski Angle and Crabbed Waist*. Technical report LNF-07/003. Laboratori Nazionali di Frascati, 2007. URL: http://arxiv.org/abs/physics/0702033.

[11] M. Zobov et al. "Test of "Crab-Waist" Collisions at the DAFNE F-Factory". In: *Physical Review Letters* 104.174801 (2010).

[12] M. E. Biagini. "Overview of B-Factories". WEYA03. In: *Proceedings of IPAC2012*. New Orleans, USA, 2012.

[13] *SPARX-FEL Project*. URL: http://www.sparx-fel.it.

[14] S. Guiducci et al. "Baseline design of the SuperB factory injection system". In: *Proceedings of IPAC2012*. New Orleans, USA, 2012.

[15] J. E. Clendenin et al. "RF Guns for Generation of Polarized Electron Beams". In: *SLAC-Pub 11526* (2005).

[16] F. Poirer et al. "Positron Production and Capture Based on Low Energy Electrons for SuperB". TUPEB057. In: *Proceedings of IPAC2010*. Kyoto, Japan, 2010.

[17] Luigi Palumbo and James Rosenzweig, editors. *Technical Design Report for the SPARC Advanced Photo-injector*. Laboratori Nazionali di Frascati, Rome, Italy, 2004. URL: http://www.lnf.infn.it/acceleratori/sparc/.

[18] Many Authors. *Linac Coherent Light Source (LCLS) Conceptual Design Report*. Technical report UC-414. SLAC-R-593, 2002.

[19] L. Zang et al. "KEKB linac wakefield studies of comparing theoretical calculation, simulation and experimental measurement". In: *Proceedings of IPAC2011*. San Sebastián, Spain, 2011.

[20] Edmund Wilson. *An introduction to Particle Accelerator*. Oxford, 2001.

[21] J. Rossbach and P. Schmüser. "Basic course on Accelerator Optics". In: *CERN Accelerator School - Fifth General Accelerator Physics Course*. Edited by S. Turner. University of Jyväskylä, Finland, 1992.

[22] F. Christoph Iselin. *The MAD Program - Physical Methods Manual*. CERN. Geneva, Switzerland, 1994.

[23] Albert Hofmann. *The physics of synchrotron radiation*. Cambridge University Press, 2004.

[24] Philip John Duke. *Synchrotron radiation production and properties*. Oxford University Press, 2000.

[25] Jens Viefhaus. *Research with Synchrotron Radiation*. DESY Summer Student Common Lectures. 2009.

[26] F. Curtis Michel. "Intense Coherent submillimiter radiation in electron storage rings". In: *Phys. Rev. Lett.* 48.9 (1981), pages 580–583.

[27] Ya. S. Derbenev, J. Rossbach, E. L. Saldin, and V. D. Shiltsev. "Microbunch Radiated Tail-Head Interaction". In: *Tesla FEL Report* 5 (1995).

[28] M. Borland. "Simple method for particle tracking with coherent synchrotron radiation". In: *Phys. Rev. ST Accel. Beams* 4.070701 (2001).

[29] A. Novokhatski. "A New Green's Function for the Wake Potential Calculation of the SLAC S-band Constant Gradient Accelerating Section". In: *SLAC-PUB-14536* (2001).

[30] H. Sugimoto, M. Satoh, and M. Yoshida. "Design study on KEK injector linac upgrade for high-current and low-emittance beams". TUPPC021. In: *Proceedings of IPAC2012*. New Orleans, USA, 2012.

[31] Pascal Dominik Hermes. "Conception de l'Injecteur et des Diagnostics du Faisceau pour le projet SuperB". Batchelor thesis. Laboratoire de l'Accélérateur Linéaire Université Paris Sud XI, 2010.